


## Topical Review

# Ultrafast dynamics observation during femtosecond laser-material interaction

Baoshan Guo<sup>1</sup> , Jingya Sun<sup>1</sup>, YongFeng Lu<sup>2</sup> and Lan Jiang<sup>1</sup><sup>1</sup>Laser Micro/Nano Fabrication Laboratory, School of Mechanical Engineering, Beijing Institute of Technology, Beijing, 100081, People's Republic of China<sup>2</sup>Department of Electrical and Computer Engineering, University of Nebraska-Lincoln, Lincoln, NE 68588-0511, United States of AmericaE-mail: [jianglan@bit.edu.cn](mailto:jianglan@bit.edu.cn)

Received 18 July 2019, revised 6 August 2019

Accepted for publication 10 August 2019

Published 20 September 2019



## Abstract

Femtosecond laser technology has attracted significant attention from the viewpoints of fundamental and application; especially femtosecond laser processing materials present the unique mechanism of laser-material interaction. Under the extreme nonequilibrium conditions imposed by femtosecond laser irradiation, many fundamental questions concerning the physical origin of the material removal process remain unanswered. In this review, cutting-edge ultrafast dynamic observation techniques for investigating the fundamental questions, including time-resolved pump-probe shadowgraphy, ultrafast continuous optical imaging, and four-dimensional ultrafast scanning electron microscopy, are comprehensively surveyed. Each technique is described in depth, beginning with its basic principle, followed by a description of its representative applications in laser-material interaction and its strengths and limitations. The consideration of temporal and spatial resolutions and panoramic measurement at different scales are two major challenges. Hence, the prospects for technical advancement in this field are discussed finally.

Keywords: ultrafast dynamics, pump-probe shadowgraphy, ultrafast continuous optical imaging, 4D ultrafast scanning electron microscopy, femtosecond laser manufacturing

(Some figures may appear in colour only in the online journal)

## 1. Introduction

Ultrafast lasers can change the states and properties of materials through interactions with them, and they can be used to control the processing of materials from the micrometer scale down to the nanometer scale or across scales [1]. Femtosecond lasers tend to impose extreme conditions in their interactions with target materials because of the ultrashort pulses (approximately  $10^{-15}$  s) and ultrahigh power

intensity ( $>10^{14}$  W cm<sup>-2</sup>) involved, and they can be focused onto nanometer spatial dimensions (approximately  $10^{-9}$  m). Because of the extreme characteristics, femtosecond lasers can be used to process almost any material with high quality and high precision as well as to process complex three-dimensional structures, which has emerged as a new frontier in the development of laser manufacturing technology. Due to its nonlinear (e.g. multiphoton) absorption, a femtosecond laser can overcome the limitations of traditional processing methods; and the accuracy of femtosecond laser fabrication currently stands at 1/50 of the diffraction limit [2]. The nonequilibrium (e.g. interelectron nonequilibrium and electron-to-lattice nonequilibrium) absorption and nonthermal phase transitions (e.g. Coulomb explosion and electrostatic



Original content from this work may be used under the terms of the [Creative Commons Attribution 3.0 licence](https://creativecommons.org/licenses/by/3.0/). Any further distribution of this work must maintain attribution to the author(s) and the title of the work, journal citation and DOI.

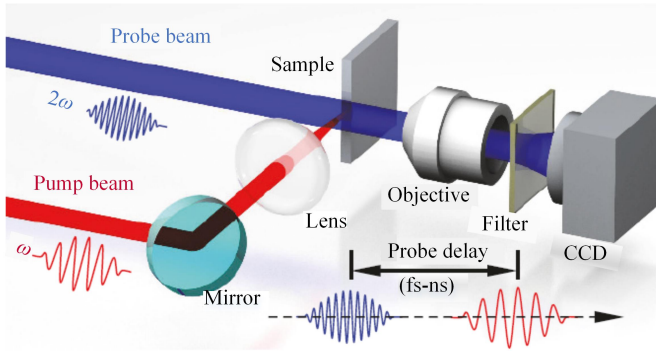


**Figure 1.** Schematic of the time-resolved pump-probe shadowgraphy setup. Reproduced from [30]. CC BY 4.0.

stripping) of femtosecond lasers can minimize heat-affected zones, cracks, and recast layers, thus improving the processing quality considerably [3, 4]. Moreover, no mask, vacuum, or corrosive gas is required in femtosecond laser fabrication. The process generates small quantities of waste compared to traditional methods and does not cause pollution. The characteristics of femtosecond lasers have led to the development of new manufacturing concepts, mechanisms, methods, and techniques that support a large number of manufacturing applications in fields such as information technology, biotechnology, pharmaceuticals, aerospace, and environmental industries [5–11].

The mechanism of femtosecond laser fabrication, including the phase change and material removal, are essentially determined by laser-electron interactions [12]. During femtosecond laser fabrication, photons are mainly absorbed by electrons, and the subsequent energy transfer from electrons to ions is of the picosecond order. Consequently, lattice motion is negligible within the femtosecond pulse duration, whereas femtosecond photon-electron interactions dominate the entire fabrication process [12]. Therefore, the regulation of laser-electron interactions or localized transient electron dynamics is critical to the development of femtosecond laser manufacturing, which makes measurement and control at the electron level challenging during fabrication processes. To understand and control the ultrafast dynamic processes, many observation techniques have been developed.

The pump-probe technique is widely used to capture the aforementioned ultrafast dynamics through repeated measurements and to study the dynamic processes of various materials in femtosecond laser manufacturing (section 2). In addition to capturing ultrafast phenomena that are either nonrepeatable or difficult to reproduce, many ultrafast continuous optical imaging techniques have been developed in recent years that can acquire a sequence of temporally and spatially resolved data from a single ultrafast event (section 3). To extract weak signals and improve spatial resolution, four-dimensional scanning ultrafast electron microscopy (4D S-UEM) systems have been employed to observe the local instantaneous electron dynamics under excitation with ultrafast laser pulses. The systems have also been used to reveal the mechanism of the diffusion, migration, or depletion behaviors of surface carriers as well as the

influence of the mechanism on the formation and modification of materials and the energy transfer process (section 4). In the following three sections of this review, we comprehensively survey the aforementioned cutting-edge measurement techniques. Some techniques were omitted in view of the limitation on article length. For example, ultrafast detectors, such as ultrafast framing cameras or streak cameras [13], are not discussed. The in-depth description of each technique in this paper begins with its basic principle, followed by a description of its representative applications in femtosecond laser manufacturing as well as its strengths and limitations. In the concluding section of this review, a summary and an outlook are provided.

## 2. Time-resolved pump-probe shadowgraphy techniques

Unlike traditional long-pulse laser fabrication, femtosecond laser fabrication essentially changes the mechanism of laser-material interaction. Currently, many fundamental questions concerning the origin of the material removal process under the extreme nonequilibrium conditions imposed by femtosecond laser irradiation remain unanswered. This affects the quality, accuracy, efficiency, and controllability of femtosecond laser fabrication and limits the extension of femtosecond laser micro- and nanofabrication techniques and applications.

To acquire laser-induced plasma dynamics, several diagnostic techniques have been developed [14–17], among which the time-resolved pump-probe shadowgraphy technique with micrometer spatial resolution and femtosecond temporal resolution has been widely employed. In a pump-probe method, a pump pulse excites a material, and a second pulse probes the pumped material. By acquiring time-delayed frames, one can reconstruct an ultrafast movie of the time-evolution reaction of the material. In particular, shadowgraphy images of transient plasma structures and material ejection provide more information than the probe beam deflection technique that can only acquire light intensity refracted by a density disturbance, and offer insights into thermal and nonthermal laser ablation mechanisms [18–22]. Further analysis of the time-dependent plasma expansion and the subsequent shockwave process according to the point explosion theory can help estimate the energy conversion, as demonstrated in previous studies for silicon ablation [23, 24]. In addition, shadowgraphy images provide insights into the plasma dynamics generated under different ablation conditions, such as different thicknesses of thermally grown oxide films [25, 26], air pressures [27], and excitation of air plasma at high laser intensities [28, 29]. In this review, we focus on the (I) observation of electron density dynamics over shaped pulses and (II) evolution of laser-induced plasma and shockwave expansion controlled by femtosecond laser pulse trains.

### 2.1. Experimental setup

Figure 1 displays a schematic of the time-resolved pump-probe shadowgraphy experimental setup [30]. The pulse from a

**Figure 2.** (a) Two-dimensional transmission mapping and electron density evolution at the centers of filaments induced by double pulses with  $t_s = 200$  fs. The energy of both pulses was  $4 \mu\text{J}$ .  $T$  denotes the transmissivity. (b) Diagram of the filament split caused by the highly reflective surface induced by the first pulse. (c) Instantaneous reflectivity of the surface at a delay of  $t = 200$  fs from simulation. Reproduced from [38]. © 2019 The Japan Society of Applied Physics. All rights reserved.

commercial Ti:sapphire femtosecond laser was divided into two beams (pump and probe) with a beam splitter. The pump beam was focused normally onto the surface of sample material. The probe beam oriented perpendicular to the pump beam was frequency doubled by using a beta barium borate (BBO) crystal and then was used to illuminate the ablated material. The transmitted shadowgraph of the plasma and the resulting shockwave were captured by a charge-coupled device (CCD). A 400 nm bandpass filter was placed before the CCD to suppress background illumination. An optical delay line was used to control the probe delays. To study the dynamics of two-pulse ablation, a sequence of shadowgraphs during ablation was recorded, with the first and the second pulses at different probe delays.

## 2.2. Observation of the electron density dynamics over shaped pulses

The femtosecond time-resolved pump-probe shadowgraphy technique is effective for detecting the extremely fast process of electron density dynamics evolution under laser pulse irradiation. Various aspects of the filaments induced by laser pulses have been investigated, such as the peak intensity [31–33], filament length [34, 35], and deposition energy [36, 37]. However, most studies have focused on the electron dynamics induced by normal Gaussian single pulses. The research on the evolution of electron dynamics induced by shaped pulses (e.g. double pulses and multiple pulses) remains scarce [12]. Electron dynamics depends strongly on the spatial and temporal energy distribution of pulses.

Electron density dynamics over the duration of shaped pulses can be observed by varying the separation time of pulses. As displayed in figure 2, upon the arrival of the second pulse, filament split was observed. This split was attributed to the emergence of a transient high-reflective surface induced by the first pulse [38]. The simulation results indicated that the reflectivity at the center of the pulse exceeded 0.8, which caused the

second pulse to be reflected strongly. However, in the pericentral area of the pulse, the reflectivity decreased rapidly. This enabled the second pulse to enter the sample and induce two shallow filaments. The experimental results indicated that the energy deposition efficiency can be optimized by shaping the laser pulses temporally, which benefits the fabrication process. After the experiments, atomic force microscopy was used to characterize the ablation morphology.

The laser-induced plasma evolution through multipulse ablation and the effect of a prepulse-induced crater on the subsequent laser field were studied using the time-resolved pump-probe shadowgraphy technique [39]. Filament splitting was observed in the early stages of plasma evolution (before  $\sim 300$  fs) (figure 3). This phenomenon was attributed to the competition between laser divergent propagation induced by a prepulse-induced crater and the nonlinear self-focusing effect. This was further validated through simulation results. Filament splitting occurred in the early stages of plasma evolution because the subsequent laser field was reshaped by the prepulse-induced crater.

Furthermore, the evolution of laser-induced plasma in fused silica has been studied with increasing numbers of pulses. Figure 4 displays the time-resolved transmission of femtosecond-laser-induced plasma with 10–300 pulses at 900 fs. As the pulse number was increased, a hole formed gradually with two side branches. The depth of the hole increased, and the side branches were formed gradually. When the pulse number was higher than 200, the peak electron density was saturated. This behavior can be attributed to the invariability of the side branches. Therefore, the focused laser formed laser-induced plasma with the same field, which ensured that the peak electron density approached a saturation point and did not change. The experimental results revealed that energy distribution of subsequent pulses could be influenced by a prepulse-induced structure. This is essential for understanding the mechanism of laser-material interaction, especially in ultrafast multiple-pulse laser ablation.

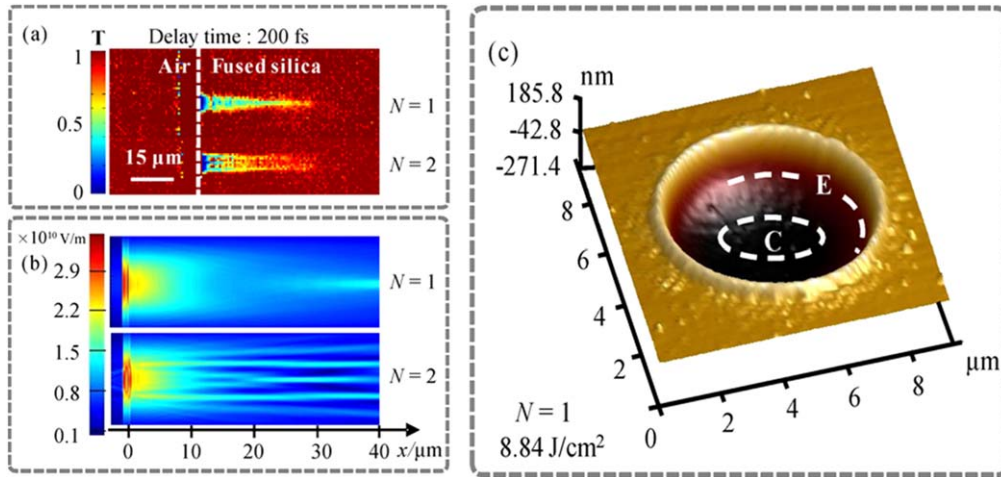


**Figure 3.** (a) Time-resolved transmission of femtosecond-laser-induced plasma caused by the first pulse ( $N = 1$ ) and second pulse ( $N = 2$ ) in fused silica with a fluence of  $8.84 \text{ J cm}^{-2}$  at 200 fs; (b) finite-difference time-domain simulation of the laser field considering the Kerr effect in fused silica with the first and second pulses; and (c) AFM morphology of the crater caused by the first pulse, where ‘E’ and ‘C’ denote the edge and the center area of the crater, respectively. Reproduced with permission from [39]. © 2019 Optical Society of America.

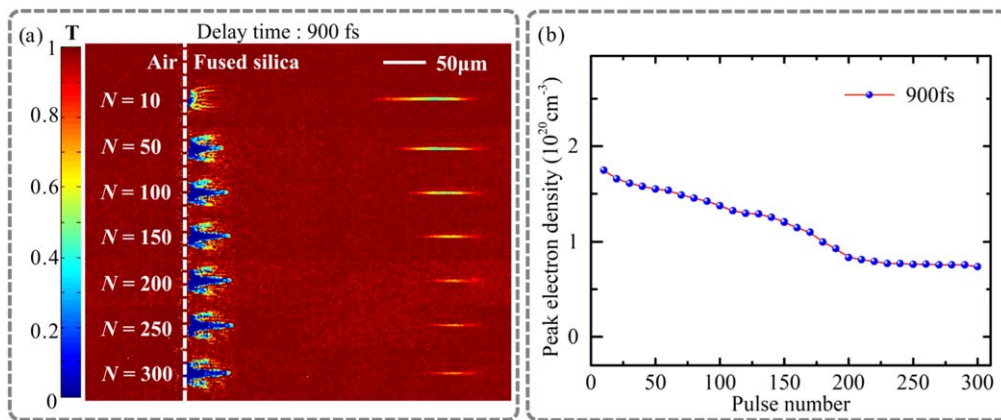


**Figure 4.** (a) Time-resolved transmission of femtosecond-laser-induced plasma in fused silica with 10–300 pulses and (b) peak electron density evolution at 900 fs with a fluence of  $17.68 \text{ J cm}^{-2}$ . Reproduced with permission from [39]. © 2019 Optical Society of America.

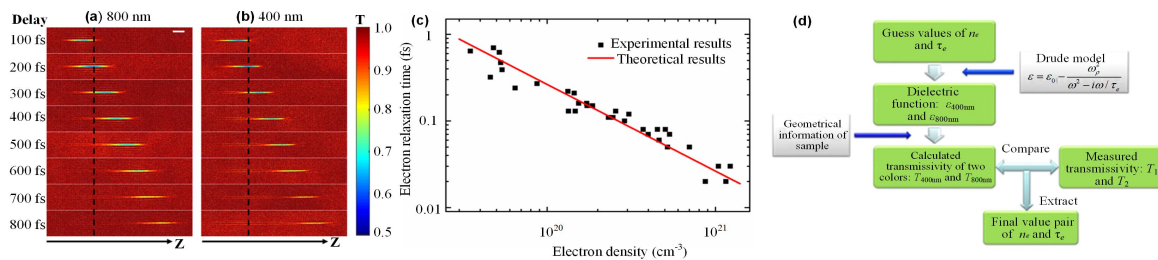


**Figure 5.** Time-resolved transmissivities of the femtosecond-laser-induced region in fused silica with (a) 800 nm and (b) 400 nm probe pulses at delay times of 100–800 fs. The pump pulses of both (a) and (b) propagate from left to right. The color map is selected to enhance transmissivity changes and plasma evolution after laser pulse irradiation. The scale bar is  $20 \mu\text{m}$ . The black lines with arrows denote the propagation direction of the pump pulses. (c) Evolution of the electron relaxation time with the electron density. The black squares denote the measured pairs of  $n_e$  and  $\tau_e$ . The red solid line represents the theoretical results obtained using the electron–ion scattering equation. (d) Schematic of the method for determining the dielectric function. Reprinted from [45], with the permission of AIP Publishing.

The electron relaxation time ( $\tau_e$ ), which is an important parameter for understanding plasma properties, should be a variable according to theoretical calculations [40–42]. However, in many experimental treatments,  $\tau_e$  has simply been

considered a constant [43, 44]. The calculation or measurement of  $\tau_e$  remains challenging. Hence, the spatiotemporal evolution of femtosecond-laser-induced electron plasma in fused silica was studied using the dual-frequency pump-probe



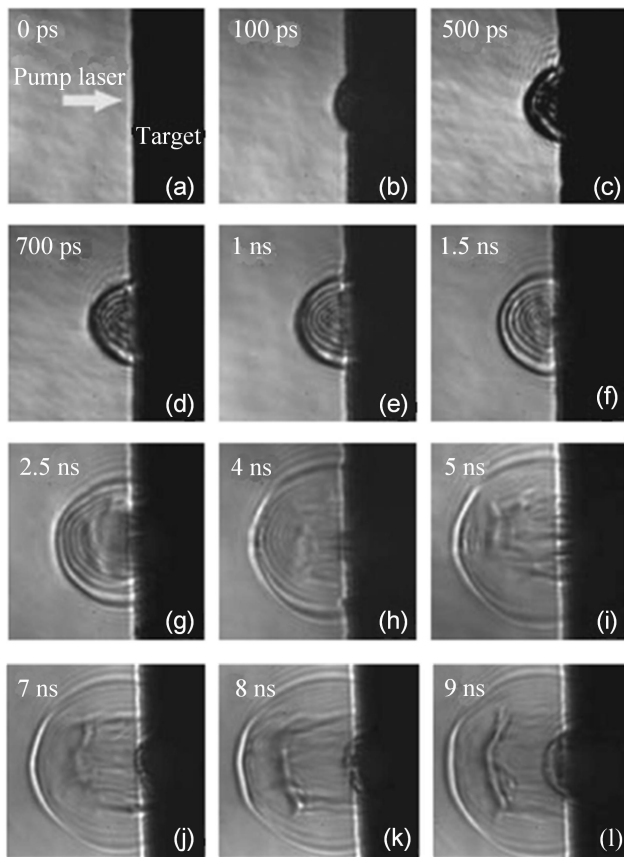


**Figure 6.** Time-resolved shadowgraphs of material ejection at indicated time delays. Reproduced with permission from [46], Copyright (2007) by the American Physical Society.

technique [45]. As displayed in figure 5, laser-induced filaments can propagate in fused silica for approximately 1 ps, which results in strong absorption of both the 800 and 400 nm probe pulses. By using the Drude model, a series of transmissivities were calculated using many pairs of  $n_e$  and  $\tau_e$  over a reasonably large scale and with high precision. The calculated transmissivities and the experimental results revealed the optimized electron density and the electron relaxation time of plasma in different parts of the filament at different delay times.

### 2.3. Laser-induced plasma and shockwave expansion

The fundamental mechanisms of ultrafast laser ablation have been explained by various theories, such as Coulomb explosion, phase explosion, and the effect of a thermoelastic wave. Ultrafast laser ablation is a composite physical process that depends on the laser parameters and the properties of the target. Regarding metal targets, the dynamic process of ultrafast laser ablation of aluminum with an energy fluence considerably higher than the ablation threshold was investigated in [46]. As displayed in figure 6, a stripe pattern preceding phase explosion can be observed in the shadowgraph with a time delay of 1 ns. For longer time delays, the contrast of the stripe pattern decreases gradually. Intermittent material ejections can be observed within the

ejected plume after 2.5 ns and longer time delays. Such ejections have not been observed for semiconductor or dielectric materials (e.g. silicon and glass samples).

The generation of femtosecond-laser-induced surface structures upon the irradiation of multiple pulses is strongly correlated with the pulse number, which in turn considerably affects successive laser-material interactions. The dynamics of plasma and shockwave expansion during the ablation of fused silica with two femtosecond laser pulses was studied with time-resolved shadowgraph imaging [29]. The experimental results revealed that during irradiation of the second pulse on the crater induced by the first pulse, the expansion of the plasma and shockwave were enhanced in the longitudinal direction (figure 7). This enhancement was attributed to the crater with concave lens-like morphology, which can considerably reflect and refocus the latter part of the laser pulse to induce strong air breakdown (figure 8).

A similar enhancement phenomenon was detected in the two-pulse ablation of silicon. To further verify the fundamental mechanism, time-resolved shadowgraphy of silicon ablation was recorded at the femtosecond timescale to directly visualize the excitation of air plasma induced by the reflected laser during the irradiation of the second pulse [30]. Moreover, the interaction between air plasma and silicon plasma was studied at the picosecond–nanosecond timescale. The study of the interaction indicated that the air plasma channel can affect the expansion dimension of the plasma and shockwave in the longitudinal direction; however, the interaction did not affect the morphology and expansion distance (figure 9).

In addition to the studies on femtosecond two-pulse ablation, recent studies have proposed that the morphology of the laser-induced crater roughens as the pulse number ( $N$ ) increases [47–50]. This phenomenon leads to a loss of laser-refocusing ability, and it can considerably alter the nature of expansion of the plasma and shockwave. To study the effect of structure evolution on the dynamics of the plasma and shockwave, time-resolved shadowgraphs were recorded during ablation with multiple pulses. Figure 10 displays the typical shadowgraphs of the plasma and shockwave during ablation with the third, fourth, and fifth pulses. Two fundamental mechanisms of plasma and shockwave expansion were revealed: the excitation of air plasma and laser-material coupling. The two mechanisms were strongly dependent on the laser-induced surface structure. When the pulse number was small, a smooth crater was generated by prior pulses, which could reflect and refocus the next pulse, thus inducing an increased laser intensity above the sample surface. Consequently, air plasma was excited and it dominated the anisotropic expansion of the silicon plasma and shockwave. When the number of pulses was large, the smooth crater roughened due to it being covered with microstructures and nanostructures. Consequently, the crater was unable to refocus the incident pulse. In this scenario, the air plasma vanished and laser-material coupling was the core mechanism of the expansion of the silicon plasma and shockwave with strong isotropic characteristics. The findings are of fundamental importance for obtaining deep insights into the nature of ultrafast laser-material interaction.

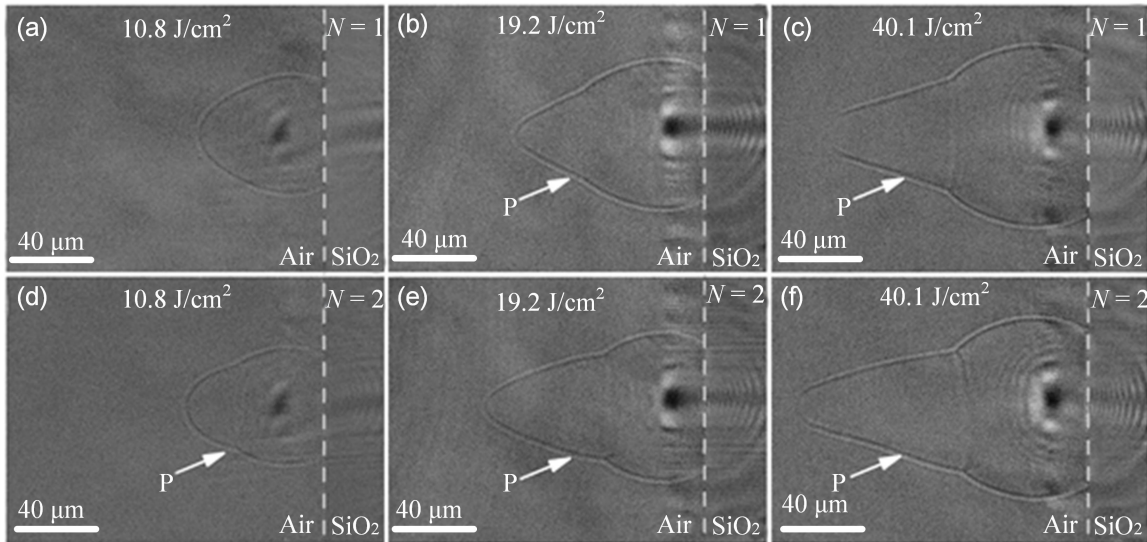


**Figure 7.** Shadowgraphs of the plasma and shockwave generated by femtosecond laser irradiation on fused silica with laser fluences of 10.8, 19.2, and 40.1 J cm<sup>-2</sup>. (a)–(c) Images recorded after the first pulse ( $N = 1$ ) and (d)–(f) images recorded after the second pulse ( $N = 2$ ).  $P$  indicates the protuberance on the top of the plasma and the shockwave front. The probe delay was 16 ns. Reproduced with permission from [29]. © 2017 China Laser Press.

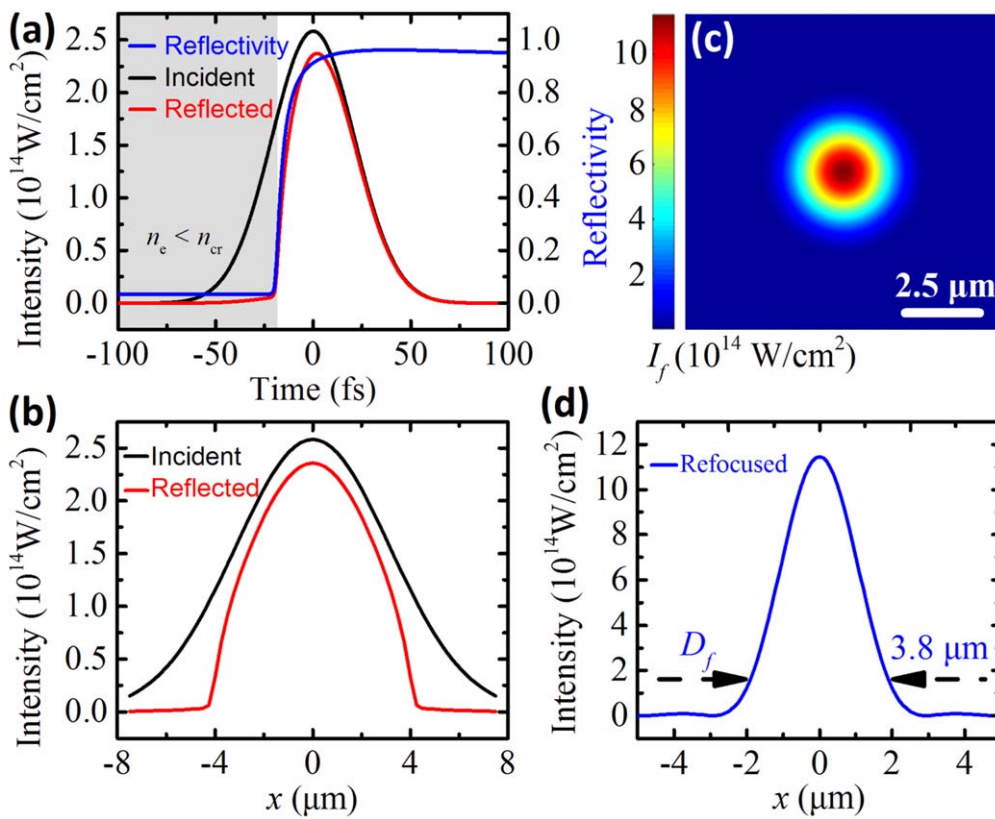


**Figure 8.** Calculation of the refocused laser intensity. (a) Time-dependence of the surface reflectivity and incident and reflected laser intensities at the beam center ( $x = 0$ ) during irradiation of the first pulse. (b) Spatial distributions of the incident and reflected laser intensities at time zero, at which the peak intensity arrived during the irradiation of the first pulse. (c) Refocused laser intensity distribution at the refocused focal plane at time zero during the irradiation of the second pulse. (d) Cross-section of the refocused laser intensity distribution at time zero. The incident laser fluence was 13.75 J cm<sup>-2</sup>. Reproduced with permission from [29]. © 2017 China Laser Press.

### 3. Ultrafast continuous optical imaging techniques

Pump-probe methods have been imperative for the study of ultrafast dynamics. However, they are inapplicable to many

ultrafast phenomena that are either nonrepeatable or difficult to reproduce, such as chaotic laser dynamics [51], optical rogue waves [52, 53], light scattering in living tissues [54], and irreversible crystalline chemical reactions [55]. Although

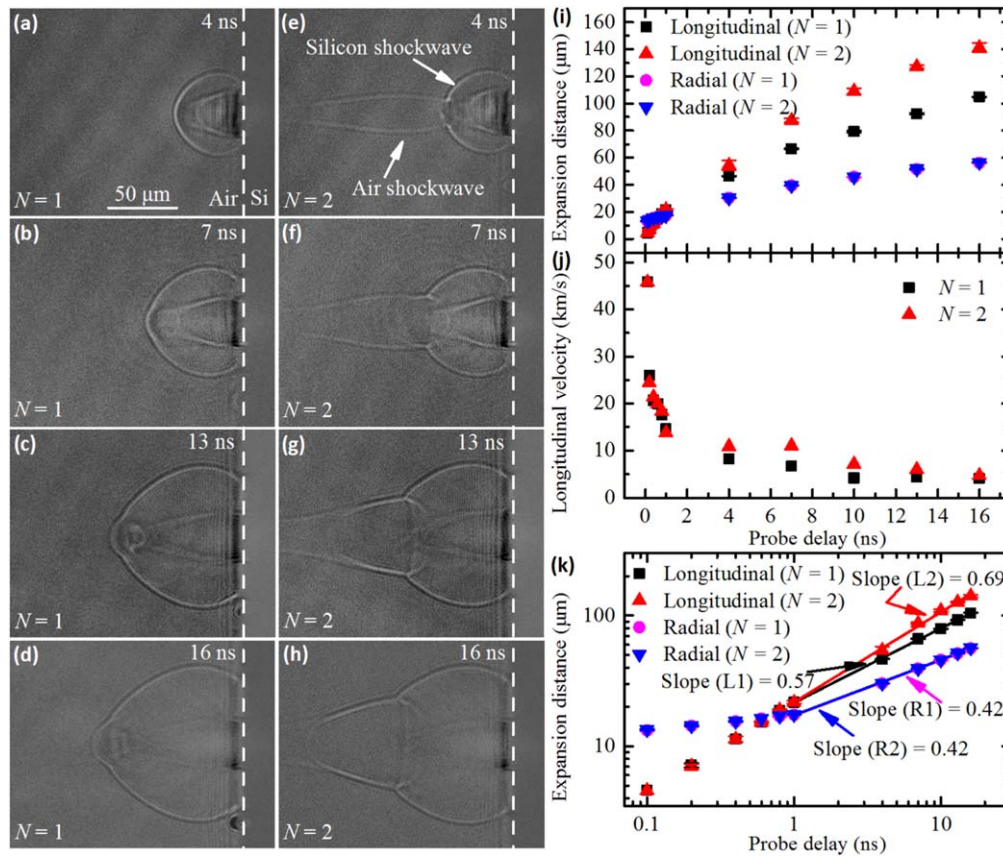


**Figure 9.** Time-resolved plasma shockwave expansion at probe delays on the nanosecond timescale. (a)–(d) Images recorded for the first pulse. (e)–(h) Images recorded for the second pulse. The dashed line represents the silicon–air interface. (i) Measurements of longitudinal and radial expansion of the silicon shockwave as a function of time for the first two pulses in the ablation of silicon. (j) Calculated longitudinal velocities of the silicon shockwave as a function of time for the first two pulses in the ablation of silicon. (k) Double logarithmic fitting of longitudinal and radial expansion for the first two pulses in the ablation. The laser fluence was  $7.27 \text{ J cm}^{-2}$ . Reproduced from [30]. CC BY 4.0.

other ultrafast phenomena are reproducible, they have significant shot-to-shot variations and low occurrence rates. Examples include dense plasma generation with ultrafast laser systems [56, 57] and laser-driven implosion in inertial confinement fusion [58]. Under these circumstances, the ultrafast continuous optical imaging techniques become necessary to overcome the limitations of pump-probe methods. In general, the techniques employ an ultrafast pulse train to record a transient event. Each subpulse in the pulse train is assigned a unique optical marker, such as different spatial positions, angles, wavelengths, states of polarization (SOPs), or spatial frequencies, which is used to separate the subpulses to recover the transient information. In the following subsections, we review four popular ultrafast continuous optical imaging techniques based on different mechanisms.

### 3.1. Ultrafast continuous imaging based on spatial division

The most direct method of continuous ultrafast imaging involves separating the imaging beams in space, which is an extension of Muybridge’s imaging setup for capturing a horse in motion [59]. In this method, an echelon is used to construct a probe pulse train, with each subpulse occupying a different spatial and temporal position (figure 11(a)). Synchronized with a high-speed process passing through the field of view

(FOV), each subpulse records the transient information of the process at a different time. The probe subpulses are projected onto different spatial areas of an image sensor, which then records the information in a continuous manner (figure 11(b)). This technique is suitable for the observation of single femtosecond laser pulse propagation. Because the intense laser pulses develop complex structures during their propagation due to self-modulation caused by nonlinear effects [60], the propagation profile is remarkably different from shot to shot even if the laser light source fluctuates marginally [61].

By using the aforementioned method, high-frame-rate observation of single femtosecond laser pulse propagation in fused silica was realized, which facilitated the determination of the influence of pulse energy fluctuation on the spatial and temporal distributions of the single laser pulse [62]. Pump-induced changes in the relative reflectivity as small as 0.2%–0.5% were observed in semimetals, which revealed both electronic and coherent phonon dynamics [63].

Figure 12(a) illustrates the schematic of the multiframe femtosecond time-resolved optical polarography (M-FTOP) system based on echelon spatial division for imaging the propagation of ultrashort pulses in an optical nonlinear medium [62]. A 65 fs, 800 nm laser pulse was split into a pump pulse and probe pulse with a beam splitter. The pump pulse was focused at approximately 1 mm inside a Kerr



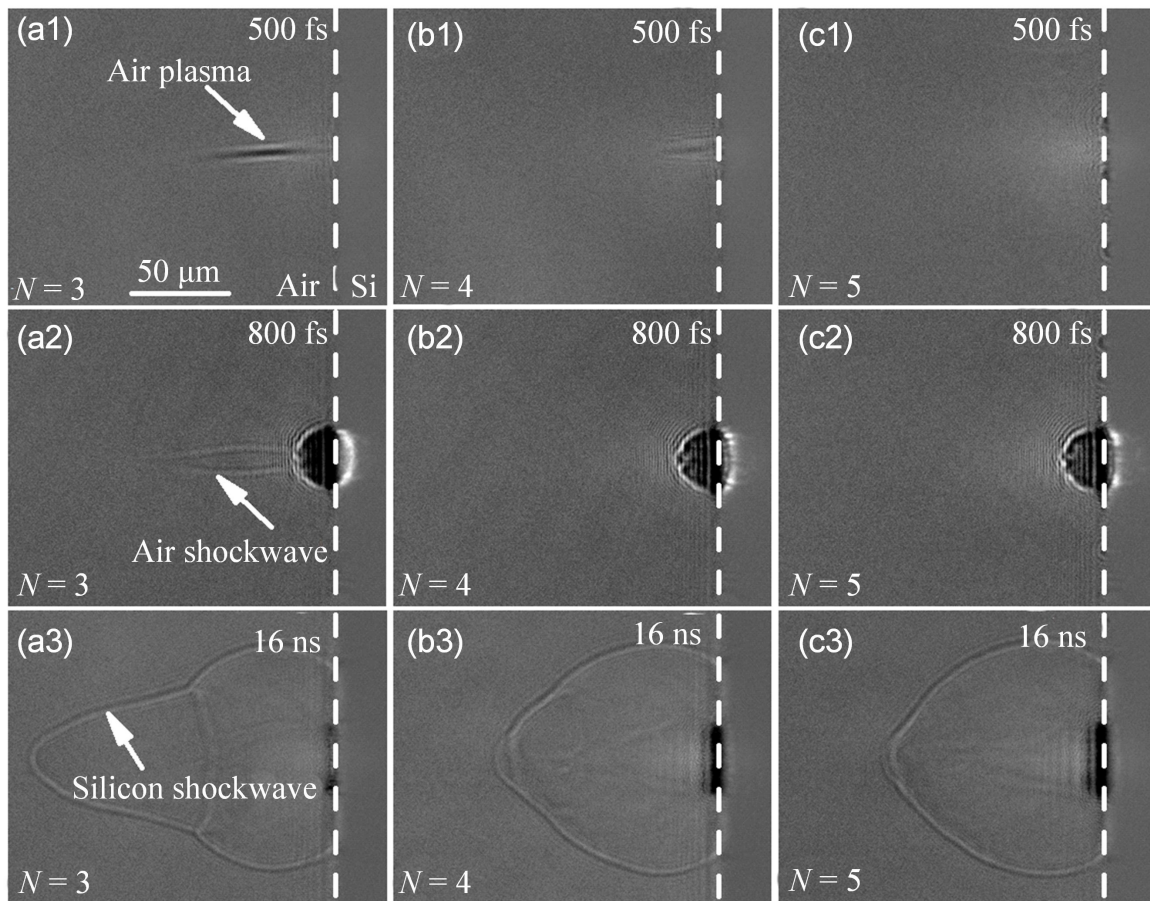


**Figure 10** Shadowgraphs of the plasma shockwave at probe delays of 500 fs, 800 ps, and 16 ns during ablation with multiple pulses. (a1)–(a3) Shadowgraphs for the third pulse. (b1)–(b3) Shadowgraphs for the fourth pulse. (c1)–(c3) Shadowgraphs for the fifth pulse. The laser fluence was  $7.27 \text{ J cm}^{-2}$ . The dashed line represents the silicon-air interface. Reproduced from [30]. [CC BY 4.0](#).

medium of fused silica glass (10 mm in length). The frequency-doubled probe pulse was incident on a four-step echelon with a step width of 0.54 mm that produced a 0.96 ps time delay for the probe pulse. The step height of 0.2 mm was consistent with the propagation of the pump pulse. The polarization axes of the two polarizers (P1, P2) placed before and after the sample were mutually perpendicular to allow the passage of parts of the probe beam. The polarography images were recorded with a high-spatial-resolution CCD camera [64].

Figure 12(b) displays the sequence images in which the spatial resolution of the pump pulse ( $45 \mu\text{J}$ ) propagation dynamics in fused silica was approximately  $4.3 \mu\text{m}$ . The frame interval was approximately 0.96 ps (corresponding to a frame rate of approximately 1.05 THz). First, the lateral size of the pump pulse spot changed marginally, which indicated filament generation because of the balance between the Kerr self-focusing and plasma defocusing effects induced by nonlinear ionization [65]. Specifically, the formation of double filaments during the propagation of the pump pulse was indicated by the profile images of the two peaks [61]. Second, the pulse profiles varied from shot to shot due to fluctuations in the pulse energy distribution, which highlights the necessity of continuous ultrafast imaging. Because intense pump pulse propagation can

lead to the generation of complex structures due to nonlinear effects [61], the propagation profile differs markedly from pulse to pulse even if the laser pulse fluctuates only marginally, which is almost impossible to observe with the pump-probe technique.

The temporal resolution of the imaging system can be improved by increasing the echelon step width; however, it remains limited by the probe pulse duration, which depends on the advancement of attosecond laser science [66, 67]. However, M-FTOP has a few insurmountable shortcomings. First, the discrete probe pulses are generated by the step echelon. Hence, the frame number determined by the step number is limited by the power of a single pulse. More importantly, the spatially discrete probe pulses can only image ultrafast dynamics with nonoverlapping trajectory. However, observation of the localized electron dynamics in the same area is of considerable importance for researching the mechanism of laser fabrication.

### 3.2. Ultrafast continuous imaging based on temporal wavelength division

Recently, a new type of ultrafast continuous imaging method based on temporal wavelength division was proposed to overcome the shortcomings of the spatial division system



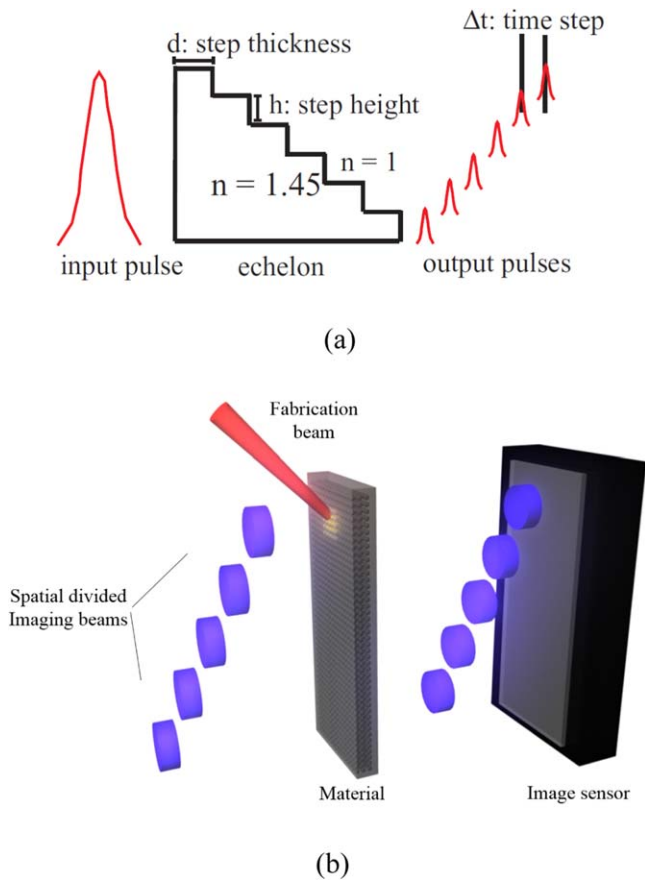


**Figure 11.** (a) Generation of time-delayed probe pulses through an echelon. Probe beams passing through thick echelon steps were retarded relative to those passing through thin steps. (b) Schematic illustration of ultrafast imaging based on spatial division.

[68]. This method employs different wavelengths of individual pulses to form imaging pulse trains, which are appropriate for observing electronic dynamic control processing (figure 13). The spatial mapping system on the detection side employs dispersive optical elements to spectrally separate probe pulses and project them onto an image sensor.

On the basis of time-stretch imaging [69–71], a representative technique of temporal wavelength division called sequentially timed all-optical mapping photography has been developed [72]. A 70 fs and 810 nm pulse was first passed through a temporal mapping device comprised of a pulse stretcher and pulse shaper. Different lengths and dispersing materials were used as pulse stretchers to control the chirp of the pulse spectrum. Then, a pulse train containing six wavelength-encoded subpulses was generated with the pulse shaper to probe dynamic scenes. The reflected or transmitted signal subpulses were passed through a spatial mapping unit, which employed a diffraction grating and an array of periscope mirrors to separate the signal subpulses in space (upper-right inset in figure 14). Finally, the spatially separated subpulses were recorded at different areas for each frame on an imaging sensor.

The STAMP system has been applied to visualize early-stage femtosecond-laser-induced plasma dynamics with a frame interval of 15.3 ps (corresponding to 65.4 Gfps) and

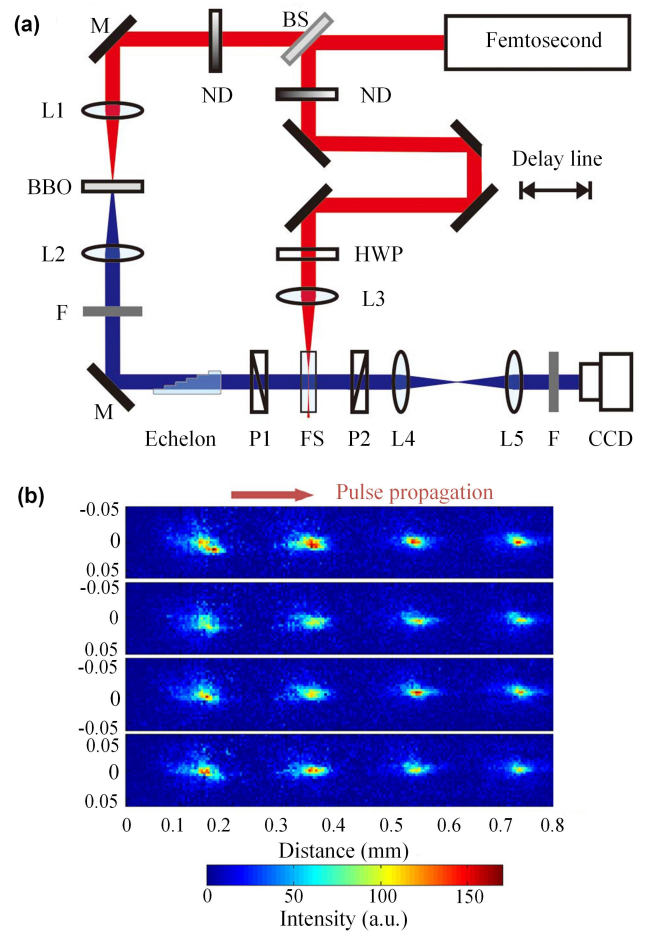


**Figure 12.** (a) Schematic of the M-FTOP imaging system based on space division. (b) Continuous observation of different laser shot dynamics under the same conditions. Reproduced with permission from [62]. © 2014 Optical Society of America.

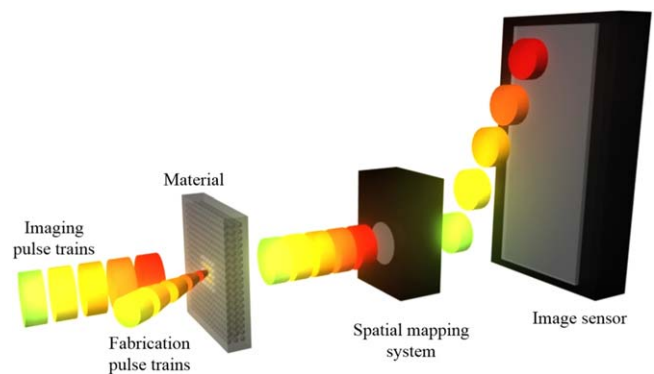


**Figure 13.** Schematic illustration of the ultrafast imaging method based on temporal wavelength division.

exposure time of 13.8 ps (figures 14(a) and (b)). In an experiment with this system, an ablating laser pulse with a pulse energy of 100  $\mu\text{J}$  and pulse duration of 70 fs was focused on the surface of a glass plate. The plasma plume generated by the femtosecond laser expanded rapidly along the radial direction, and the speed of the plume front was calculated to be approximately  $10^5 \text{ m s}^{-1}$ .

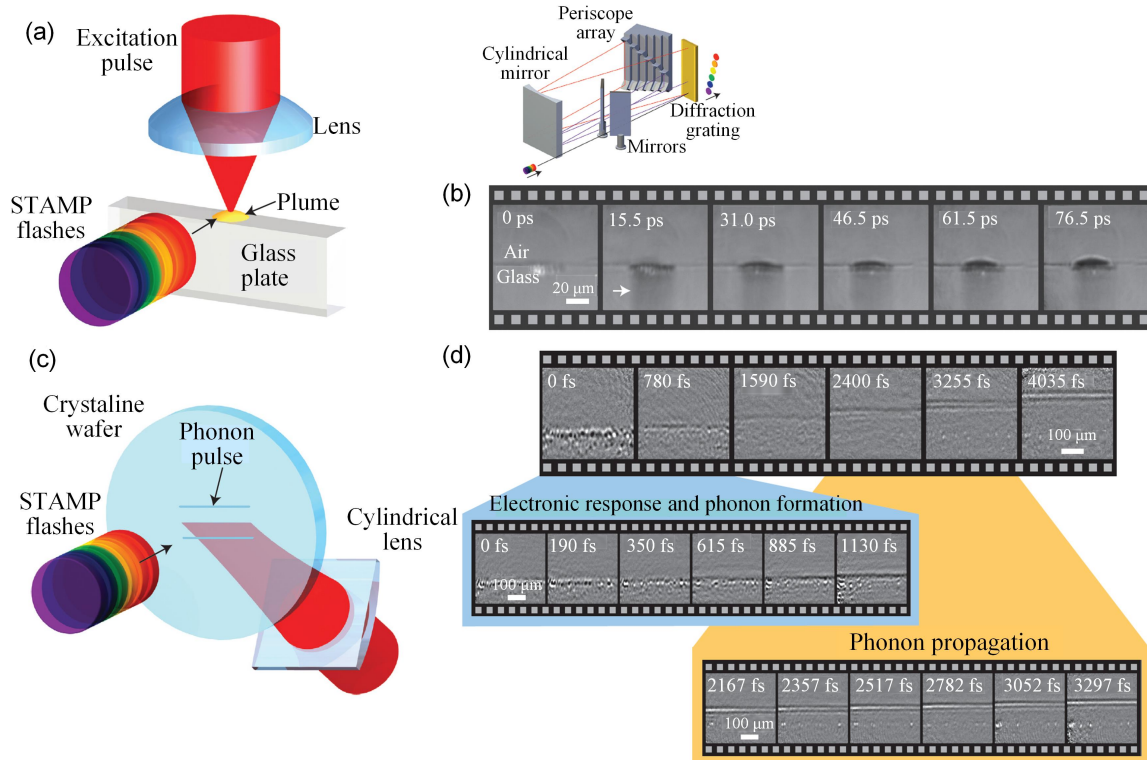


**Figure 14.** STAMP. (a) Schematic of plasma dynamics observation. (b) Continuous imaging of plasma dynamics with STAMP. (c) Schematic of phonon dynamics observation. (d) Continuous imaging of phonon dynamics with STAMP. Inset: A spatial mapping unit employing a diffraction grating and an array of periscope mirrors to separate pulse trains in space. Reprinted by permission from Macmillan Publishers Ltd: Nature Photonics [72], Copyright 2014.

Moreover, STAMP has been used to observe phonon dynamics at the femtosecond time scale (figures 14(c) and (d)). An excitation pulse (pulse energy:  $40 \mu\text{J}$ ) was line-focused onto a ferroelectric crystal ( $\text{LiNbO}_3$ ) wafer at room temperature to produce a coherent phonon-polariton pulse through impulsive stimulated Raman scattering. The phonon pulse formation was captured with a frame interval of 812 fs (corresponding to 1.23 Tfps) and exposure time of 1020 fs. Frames from a STAMP movie of the phonon dynamics are displayed in figure 14(d). The frames illustrate the entire dynamic process, including the generation of laser-pulse-excited lattice vibrations in the crystal and the propagation of a phonon-polariton wave packet. In addition, figure 14(d) depicts the propagation of a wave packet with a frame interval of 229 fs (corresponding to 4.37 Tfps). The speed of the phonon-polariton wave packet was calculated from the acquired images to be  $4.6 \times 10^7 \text{ m s}^{-1}$  (one-sixth of the speed of light). However, the total number of frames in a single shot of this system was limited to six due to the simple embodiment of the spatial mapping system.

Subsequently, several similar techniques have been developed to reduce the complexity and improve the performance of the STAMP system [73–76]. For example, the polarization state can be used as an optical marker combined with the wavelength marker to improve the spatial mapping system [73, 76]. A spectrally filtered (SF)-STAMP system was developed with a different spatial mapping method [74, 75]. A schematic of the SF-STAMP system [74] is illustrated in figure 15(a). This system expanded the probe laser bandwidth

from 20 to approximately 40 nm and eliminated the requirement for the pulse shaper used in the temporal mapping device. Instead, the system was equipped with a frequency-chirped pulse to capture ultrafast events. The spatial mapping device was replaced with a diffractive optical element (DOE) and a tilted bandpass filter [77, 78]. The DOE can generate 25 spatially resolved replicas of the signal pulse, which are incident on the bandpass filter at different angles. Hence, different transmissive wavelengths can be selected according to the incident angles to form the imaging sequence [77]. The sequence depth can be determined according to the number of replicas produced by the DOE. The temporal resolution of imaging can be controlled through spectral dispersion; however, the resolution is limited by the transmissive wavelength range. An observation timescale from subpicoseconds (approximately  $10^{-13} \text{ s}$ ) to subnanoseconds (approximately  $10^{-10} \text{ s}$ ) can be achieved [75].

The SF-STAMP system was applied to capture the dynamics of the crystalline-to-amorphous phase transition of the  $\text{Ge}_2\text{Sb}_2\text{Te}_5$  alloy induced by a frequency-doubled pump pulse. The gradual changes in the images of 25 frames (figure 15(b)) with an average frame interval of 133 fs (corresponding to 7.52 Tfps) indicated the following: the amorphized area had decreased reflectance, and the phase change domain did not spread spatially to the surrounding crystalline area. These findings experimentally verified the theoretical phase transition model that attributed the initiation of nonthermal amorphization to the displacement of germanium (Ge) atoms from octahedral to tetrahedral sites [74, 79].

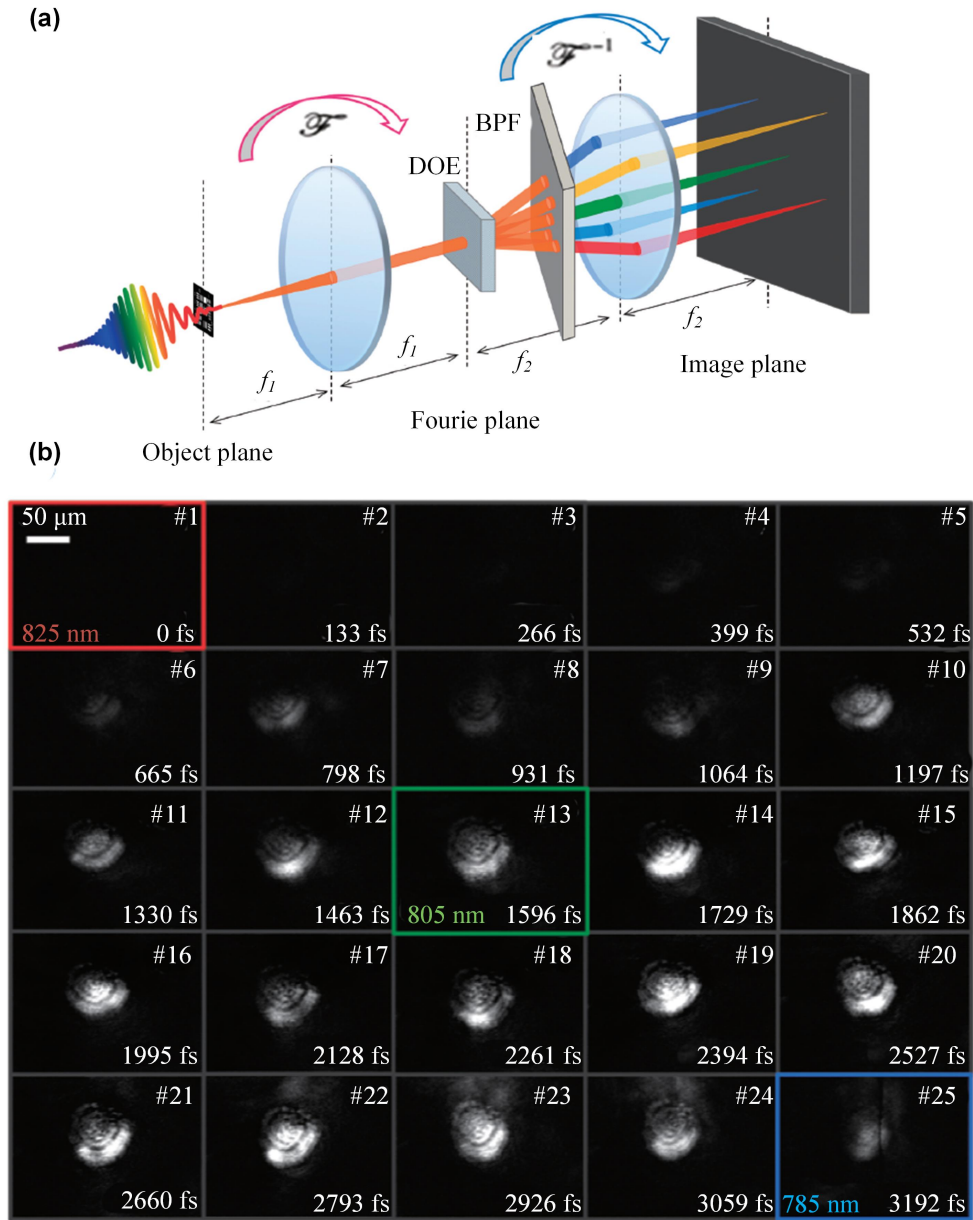


**Figure 15.** (a) Schematic setup of the spectrally filtered (SF)-STAMP system and (b) sequence images of the crystalline-to-amorphous phase transition of the  $\text{Ge}_2\text{Sb}_2\text{Te}_5$  alloy captured by the 25-frame SF-STAMP at 7.52 Tfps. Reproduced from [74]. © IOP Publishing Ltd. CC BY 3.0.

Continuous imaging of light propagation at a frame rate of 3.85 Tfps for 60 frames was achieved by combining temporal wavelength division with the compressed sensing algorithm. This technique is called compressed ultrafast spectral-temporal (CUST) photography [80]. In this imaging system, an 800 nm, 50 fs laser pulse (bandwidth: 18 nm) is stretched with a grating pair. By tuning the incident angle of the grating pair, the temporal resolution of the system can be tuned continuously from 0.1 to 5 ps. On the scene plane, the stretched pulse is transmitted through an ultrafast object and then projected onto a digital micro-mirror device (DMD). The DMD spatially encodes the signal pulse with pseudorandom binary patterns. The encoded pulse is further dispersed using a set of optics and

received onto a CCD sensor. Multiple temporally or spectrally resolved images can be reconstructed from the resulting compressed two-dimensional image by using the compressed sensing algorithm.

The frame number (60 frames) and imaging speed (7.52 Tfps) of the CUST photography system and the SF-STAMP technique, respectively, are among the highest in the ultrafast optical imaging domain. Although the light throughput of the original STAMP system is high, the system is limited by a low sequence depth. By contrast, the CUST photography system and the SF-STAMP technique have increased sequence depth at the cost of a considerable decrease in light throughput. In addition, these techniques are applicable only to ultrafast processes insensitive to the wavelength.

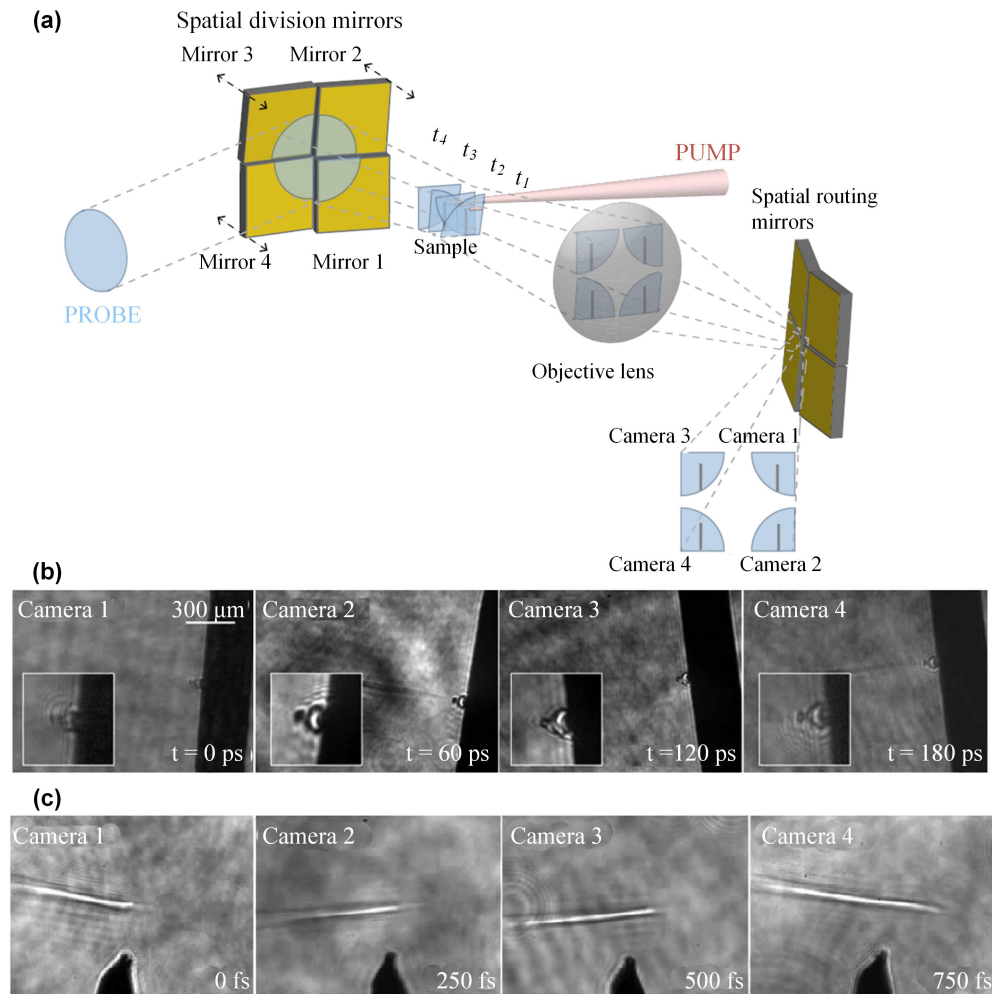


**Figure 16.** (a) Schematic of the ADMC system. The incoming probe pulse is projected onto a two-by-two mirror array that splits the probe into four sub-beams with different temporal delays. Another set of two-by-two mirror arrays is used to route the sub-beams to individual cameras. (b) Four frames of femtosecond-laser-induced plasma creation and ablation on the surface of a metal wire. (c) Four frames of a femtosecond-laser-induced ionization front propagating in air. Reproduced with permission from [81]. © 2018 Optical Society of America.

### 3.3. Ultrafast continuous imaging based on angle division

In the angle-division method, a transient event is probed from different angles to avoid the spectral problems of STAMP or CUST. For example, an angle-division-based multiple-camera (ADMC) system was developed with two sets of two-by-two mirror arrays with different angles for spatial and temporal division and routing of multiple probe pulses [81]. This single-shot scheme (figure 16(a)) was successfully applied to capture femtosecond ionization fronts propagating at the speed of light in air as well as laser-induced ablation of solid targets (figure 16(b)). The ADMC system was developed to provide individually adjustable frame intervals ranging from 30 fs to hundreds of picoseconds.

As depicted in figure 16(a), an 800 nm, 30 fs pulse is split into a pump pulse and probe pulse. The frequency-doubled probe pulse for imaging is spatially split into four beams with a two-by-two square-mirror array. Each mirror is angled marginally inward so that all beams cross the target located at a designed position from the mirror array. Moreover, each mirror is set on its own translation stage so that the temporal

delay of each beam can be adjusted individually. After passing the target plane, the four probe beams are reflected independently by another two-by-two square-mirror array, which is angled outward, and directed toward individual cameras through a single imaging lens.

The dynamics of laser-induced plasma creation and expansion are captured at the timescales of hundreds of femtoseconds to picoseconds. Figure 16(b) displays four successive frames of femtosecond-laser-induced plasma creation and ablation on the surface of a metal wire. The frames were captured at 0, 60, 120, and 180 ps. At approximately 4 ps before the arrival of the pump pulse ( $t = 0$ ), a plasma plume with a hemispherical shock boundary was formed on the surface (Camera 1). The formation of this plume was attributed to a pump pulse that arrived 10 ns before the main pump pulse. The arrival of this pump pulse is evident from the absence of an air ionization trail in the image captured by Camera 1; but the presence of an air ionization trail is seen in the images captured by Cameras 2, 3, and 4. In addition, the size of the plasma plume and the shock



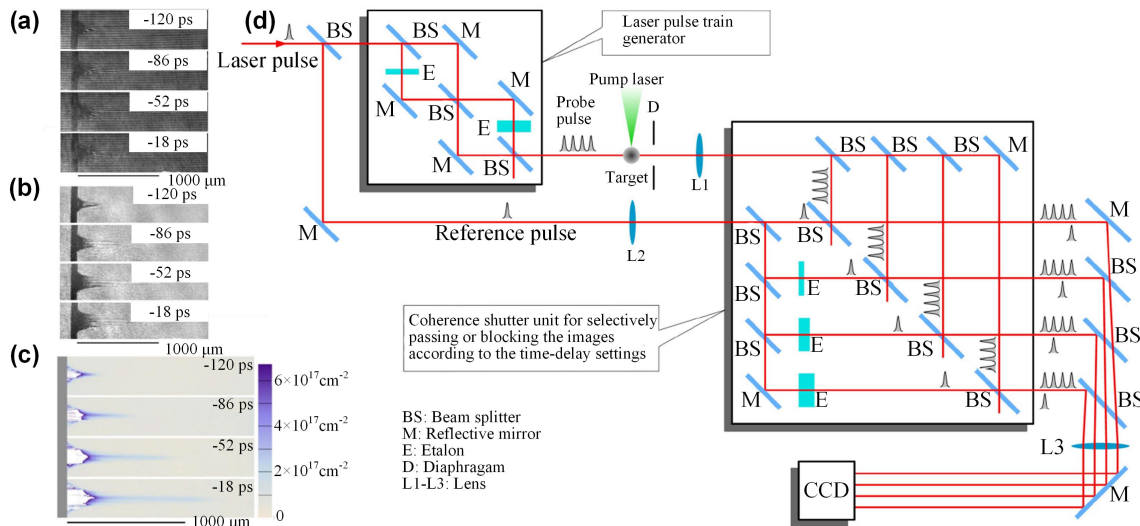


**Figure 17.** Formation of the discharge path generated by irradiating aluminum foil with a laser having a pump laser energy of 108 mJ. (a) Four holograms obtained at  $-120$ ,  $-86$ ,  $-52$ , and  $-18$  ps; (b) reconstructed light intensity images; (c) reconstructed electron areal density images; and (d) layout of the OCFI system. Reproduced with permission from [82]. © 2017 Optical Society of America.

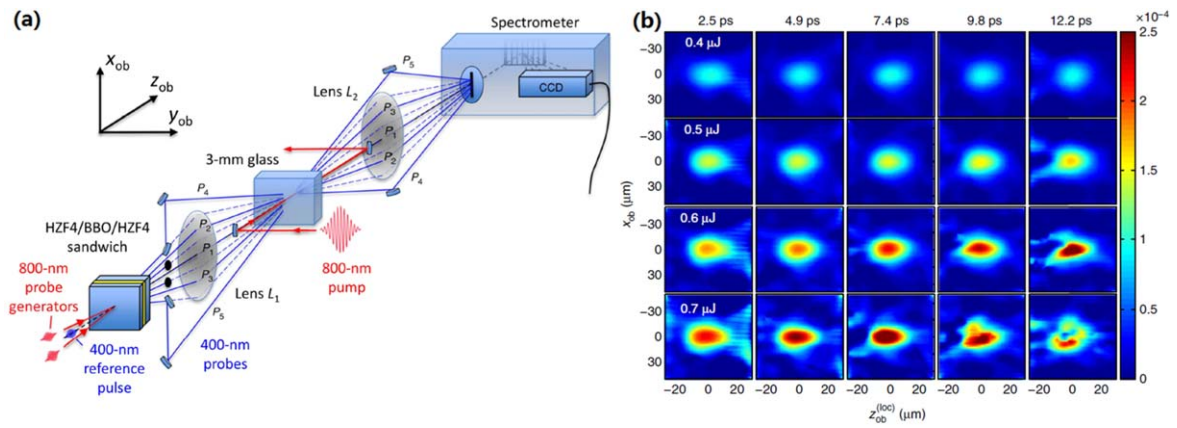
boundary did not change after 180 ps, which indicated that the plasma expanded over a considerably longer time scale, such as nanoseconds. At  $t = 60$  ps, the main pump pulse interacted with the target surface and formed a smaller plasma. Similar to the larger plasma, the smaller plasma did not change considerably over a few hundreds of picoseconds. This double plasma formation is a rare event and does not always occur in repeated experiments, which indicates the usefulness of continuous imaging diagnostics when capturing unusual ultrafast events. In addition, sequences of a femtosecond-laser-induced ionization front propagating in air were captured with a temporal resolution of 250 fs (figure 16(c)).

Another method of angle division involves extracting information at different times from interferometric images captured at different angles. Here, we introduce two representative works. One is the all-optical coaxial frame imaging (OCFI) method based on parallel coherence shutters, in which a train of laser pulses coaxially illuminates the target and generates holograms in different areas in the spatial domain [82]. With the OCFI method, nonmultiplexing serial images having high temporal and spatial resolution with identical spatial, temporal, and chromatic benchmarks can be captured in a single shot (figure 17). As displayed in figures 17(d), (a) 527 nm, 10 ps pulse is split into a probe pulse and reference pulse. The probe pulse is split into a train of four coaxial daughter pulses with a temporal interval of 34 ps with three beam splitters and two etalons. The pulse energy of each daughter probe pulse at the target is approximately  $0.1\text{--}1 \mu\text{J}$ . After passing through the target, the pulse train is split into four identical pulse trains, whereas the reference pulse is split into four pulses with different time delays. The time delay of a specific reference pulse is set to be the same as that of a specific daughter probe pulse so that each probe pulse train only interferes with a specific reference pulse and generates a unique hologram. Then, the four spatially separated holograms are projected onto four nonoverlapping areas in a CCD. Each hologram is separated spatially and

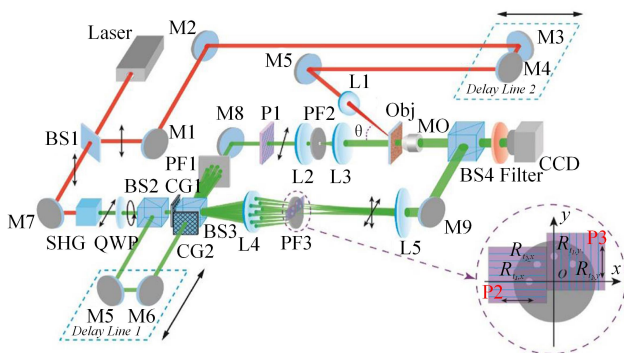
temporally from the others by using a coherence shutter without the assistance of any mechanical or optoelectronic device.

A 1064 nm, 150 ps, and 100 mJ pump pulse was focused on a  $70 \mu\text{m}$  thick aluminum foil. Pump-laser-induced ‘superfast jets’ were ejected from the ablation side (figures 17(a)–(c)), which may be considered a discharge path. The apparent velocity of the ‘jet’ front exceeded  $9000 \text{ km s}^{-1}$ . The ‘jet’ tail mainly consisted of dense plasma that blocked the probe laser and appeared as a shadow in the holograms. The light intensity images (figure 17(b)) and the electron density maps (figure 17(c)) related to the light phase were reconstructed from the holograms (figure 17(a)). The maximum electron areal density and maximum electron volume density of the ‘jet’ head were approximately  $2 \times 10^{17} \text{ cm}^{-2}$  and  $1 \times 10^{20} \text{ cm}^{-3}$ , respectively.

Figure 18(a) illustrates another angle-division system called single-shot frequency-domain tomography (SFDT) for reconstructing ultrafast spatiotemporal dynamics [83]. In this technique, an 800 nm, 30 fs pump pulse creates an evolving luminal-velocity refractive index structure in a fused silica glass due to its nonlinear refractive index and the pump-generated plasma. A three-layer structure consisting of a BBO crystal sandwiched between two HZF4 glass plates was employed to generate 15 frequency-doubled probe pulses from a pair of spatiotemporally cross-incident pulses (800 nm, 30 fs,  $30 \mu\text{J}$ ). Among the 15 probe pulses, five probe pulses with different projection angles were selected and overlapped both spatially and temporally at the target for continuous imaging of a transient, which was measured using spectral imaging interferometry [84–86]. The reference pulse recorded the phase reference and the probe pulses that interfered inside the spectrometer and projected a grid-like frequency-domain intensity pattern or hologram onto a CCD camera [87]. The evolution images were reconstructed by windowing and inverse-Fourier-transforming the hologram area associated with each probe pulse and applying the tomographic image reconstruction algorithm [83, 88].



**Figure 18.** (a) Schematic of the SFDT system based on angle division. (b) Imaging of the nonlinear index profile at four different pump energies and five different propagation times. Reprinted by permission from Macmillan Publishers Ltd: Nature Communications [83], Copyright 2014.



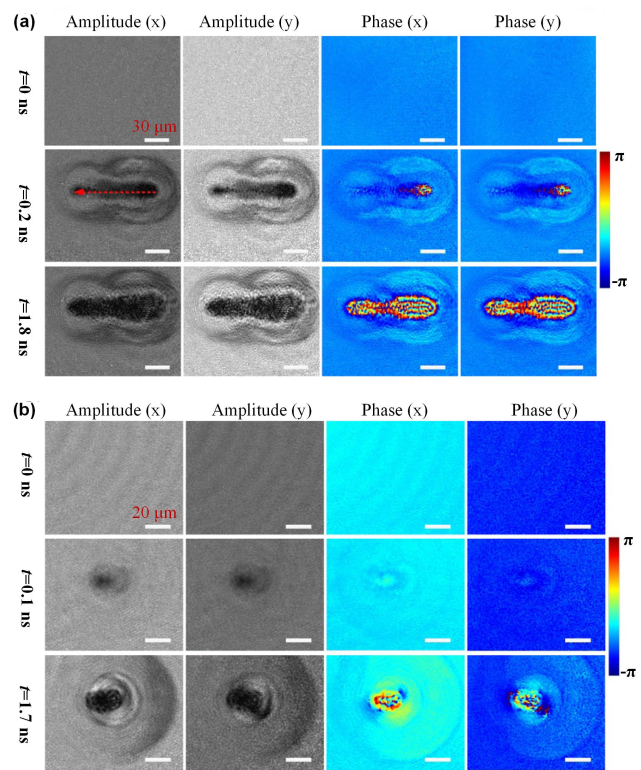
**Figure 19.** Schematic of the THPM experimental setup for imaging laser-induced damage. The black arrows indicate the pulses' SOPs. Lower-right inset: generation of four reference pulses having different spatial frequencies. Reproduced with permission from [90]. © 2017 Optical Society of America.

Figure 18(b) displays frames from SFDT movies of the evolving index profile induced by the propagation of an ultrafast laser pulse in a fused silica glass with different pulse energies. The temporal resolution of the reconstructed movie was approximately 2.5 ps. The reconstructed movie revealed a series of nonlinear dynamics, especially at high pulse energies, such as self-focusing of the pulse within 7.4 ps and the formation of a spatial lobe due to laser filamentation at 9.8 ps. In addition, the index ‘hole’ displayed in the final image at 12.2 ps indicates that the plasma generated induced a negative index change that locally offset the laser-induced positive nonlinear refractive index change.

The interferometry imaging method can record complex amplitudes and capture dynamic events along the propagation directions of probe pulses. However, the limited number of illumination angles results in artifacts that strongly affect the reconstructed images [89]. Consequently, the spatial resolution of this method is suitable for imaging simple structured objects only.

### 3.4. Ultrafast continuous imaging based on spatial frequency division

The last method in the ultrafast continuous imaging domain is spatial frequency division, which adds different spatial carrier



**Figure 20.** Time-resolved amplitude and phase contrast images of ultrafast-laser-induced damage in (a) linear polarizer and (b) mica lamina sample. Reproduced with permission from [90]. © 2017 Optical Society of America.

frequencies to different probe pulses. Through image reconstruction, spatially superimposed temporal information can be separated in the spatial frequency domain to realize ultrafast continuous imaging. Two representative techniques are discussed in the following text.

Figure 19 displays the time-resolved holographic polarization microscopy (THPM) system based on spatial frequency division for monitoring laser-induced ultrafast phenomena in polarization-sensitive materials [90]. A 1064 nm, 30 ps imaging probe pulse was frequency doubled, tuned to circular polarization, and then split into two pulses with a time delay. Each

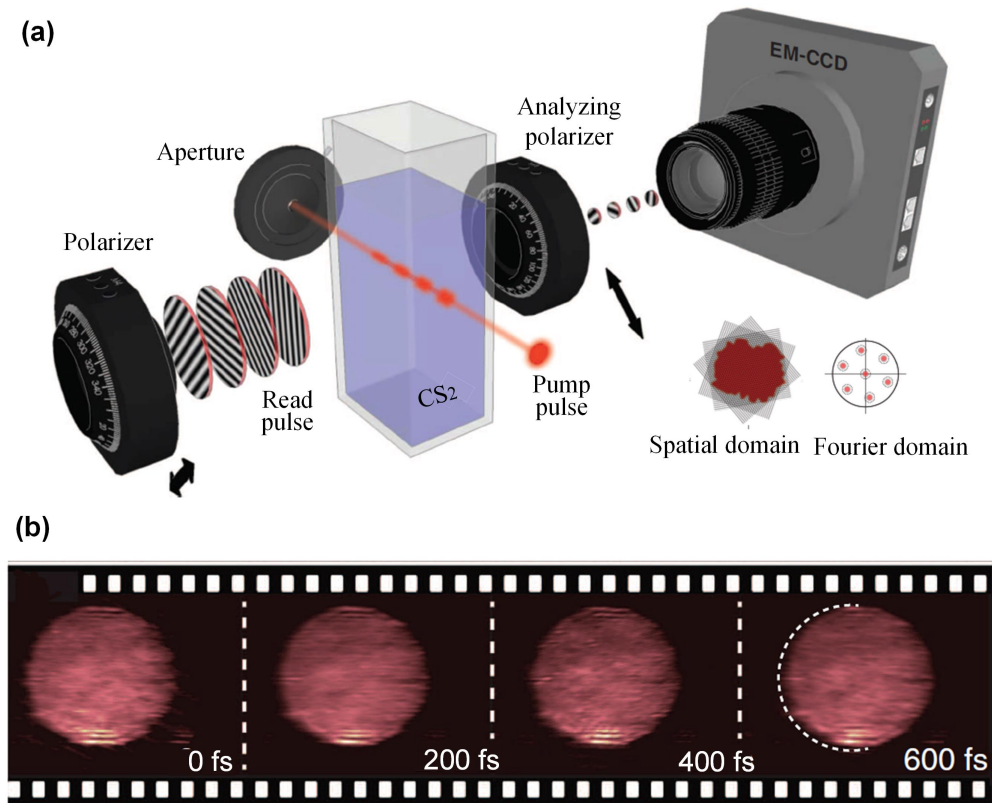


**Figure 21.** (a) System schematic of the FRAME imaging based on spatial frequency division. (b) Sequence of reconstructed frames of a propagating femtosecond laser pulse in CS<sub>2</sub> liquid. Reproduced from [95]. CC BY 4.0.

probe pulse was further split into signal pulses and reference pulses with different SOPs. Hence, two signal pulses and two reference pulses were generated and further passed through different spatial filters to load different spatial carrier frequencies. Then, the interference holograms of the signal pulses and reference pulses with different spatial frequencies were recorded with a CCD camera. Finally, the amplitude and phase information of two orthogonal polarization components of two sequential vector wavefronts with ultrashort time intervals were retrieved by performing image reconstruction [91].

THPM was applied to the real-time imaging of laser-induced damage (figure 20). A thin film linear polarizer was observed with a pump energy fluence of  $1.1 \times 10^2 \text{ J cm}^{-2}$  (figure 20(a)). The amplitude and phase distributions of two orthogonal polarization states of the object waves associated with two different time delays of 0.2 and 1.8 ns were obtained simultaneously at an imaging speed of 625 Gfps. The distributions indicated that the relative index change between the two orthogonal polarization states was nearly identical in the process of laser irradiation. In addition, a mica lamina plate was tested with a pump intensity of  $>40 \text{ J cm}^{-2}$  (figure 20(b)). The initial amplitude and phase change captured by the system at 0.1 and 1.7 ns verified the generation and propagation of shock waves and revealed nonuniform changes in the transmission and refractive indices in the process of laser irradiation because of the sample's anisotropy.

The time-resolved polarization imaging technique is imperative for investigating the ultrafast phenomena in polarization-sensitive materials because focused femtosecond laser irradiation in isotropic materials, such as fused silica [92, 93], induces artificial birefringence modification. The THPM system with an improved temporal resolution can be applied to study other ultrafast events, such as free-electron generation and lattice heating [94].

Another technique based on spatial frequency division is frequency recognition algorithm for multiple exposures (FRAME) imaging [95]. Instead of forming the interference fringes, FRAME encodes various carrier frequencies to probe subpulses through intensity modulation achieved with a Ronchi grating. By using this system, a 125 fs probe pulse was split into four subpulses. The intensity profile of each subpulse with a specified time delay was modulated using Ronchi gratings with an identical period but unique orientations (figure 21(a)). Thus, the dynamic temporal information of the scene could be captured with a CCD camera in a single shot and separated in the spatial frequency domain without any crosstalk. Finally, the image sequence could be recovered through image reconstruction according to the THPM technique. By using the FRAME imaging system, the propagation of a femtosecond laser pulse through carbon disulfide (CS<sub>2</sub>) liquid was captured with a temporal resolution of 200 fs (corresponding to an imaging speed of 5 Tfps) (figure 21(b)).



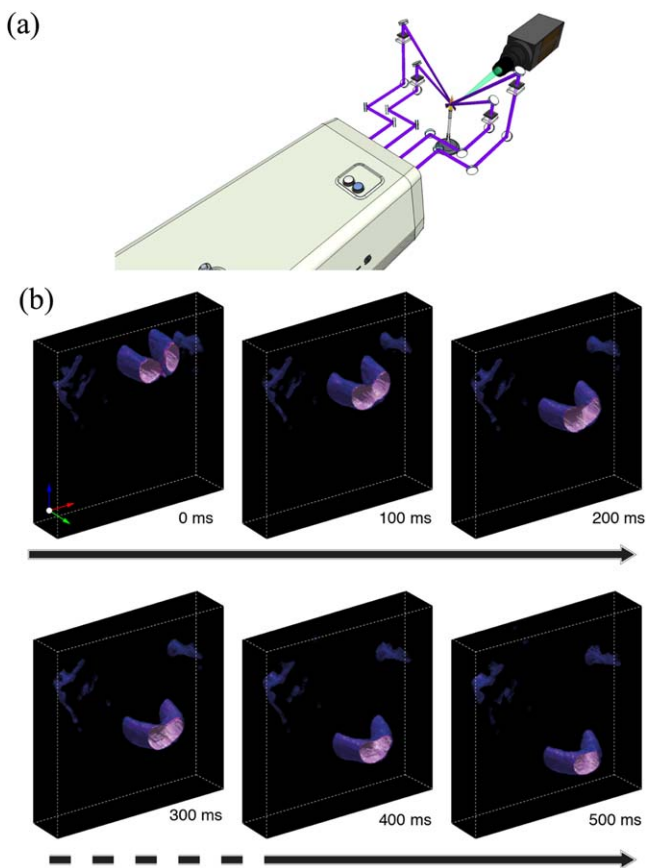


**Figure 22.** (a) Optical arrangement for the spectroscopic and laser sheet experiments conducted using FRAME. (b) Temporally resolved 3D imaging using FRAME combined with laser sheet illumination. The recorded 3D sequence displays a dye droplet falling through a cuvette with water. Reproduced from [95]. CC BY 4.0.

Because each FRAME image is extracted using a unique spatial code, the method does not rely on a specific optical wavelength or laser bandwidth. Therefore, it can be used for spectroscopic measurements or 3D imaging combined with laser sheet illumination (figure 22).

A key feature of the spatial frequency division method is the use of spatial frequency rather than dispersion to generate and separate probe pulses. Not only can wavelength-sensitive measurements be avoided but pulse spectral information can also be retained for further spectroscopic analysis. The spatial carrier frequency can be attached to the probe pulses through either interference or intensity modulation, as demonstrated using the THPM and the FRAME techniques, respectively. The THPM technique can retrieve the amplitude and phase information of ultrafast dynamics. The FRAME technique can be easily transplanted into existing imaging systems to achieve high-dimensional imaging of ultrafast events. However, the poor sequence depth achieved with the frequency division method can only be increased by sacrificing either the FOV or spatial resolution.

The nine representative techniques based on the aforementioned four main methods are summarized in table 1 in

terms of their system laser source, temporal resolution, frame number, specifications, and applications to help researchers select the most suitable technique for their specific studies.

#### 4. Second generation four-dimensional ultrafast electron microscopy

During femtosecond laser fabrication, photons are mainly absorbed by electrons, and the subsequent energy transfer from electrons to ions occurs over a time scale of picoseconds. Hence, femtosecond photon-electron interactions dominate the whole fabrication process, which poses a challenge in terms of measurement and control at the electron level during fabrication processes. Pump-probe and ultrafast continuous imaging techniques are viable solutions crucial for understanding phenomena such as electron relaxation, carrier dynamics, and charge transfer. Hence, the challenge lies in combining the atomic spatial resolution of the electron microscope with the ultrafast temporal resolution of time-resolved spectroscopy to devise a unique analytical tool that can provide dynamic information about molecular events with extremely fine detail simultaneously in both space and time. The ability to access carrier dynamics selectively on material surfaces with high temporal and spatial control in a photo-induced reaction is a particularly challenging task that can only be achieved by applying four-dimensional ultrafast electron microscopy (4D UEM) with time-resolved images that have nanometer spatial and femtosecond temporal resolutions. Although there is a problem of contamination of vacuum system by the laser ablated materials, the 4D UEM can well realize the observation of various phenomena before laser ablation. In addition, if the 4D system works in a single pulse mode, the amount of ablated materials is small and controllable. Recently, as a new direction in 4D electron microscopy, second generation ultrafast electron microscopy (S-UEM), with 650 fs and 5 nm temporal and spatial resolutions, was developed for the visualization of materials dynamics [96–100].

##### 4.1. Experimental setup of S-UEM

A description of the 4D S-UEM experimental design is given in this section to help comprehend the manner in which the measurements are realized [96]. The 4D S-UEM experimental system integrate a femtosecond Clark-MXR fiber laser with a modified FEI Quanta 650 scanning electron microscope (figure 23). The 1030 nm, 270 fs laser pulse is divided by a beam splitter and directed toward two independent harmonic generators (HGs) to produce the second and third harmonic signals, respectively. The output of the first HG (343 or 515 nm) is directed with precision through a pyrometric quartz window and is focused tightly on a cooled Schottky field-emitter tip (zirconium-oxide-coated tungsten) to generate the pulse, whereas the 515 nm output is directed onto the sample as a pump pulse to photoexcite the specimen under study. The relative timing between the two pulses is adjusted with precision through a computer-controlled optical delay



**Table 1.** Comparative summary of representative continuous ultrafast optical imaging techniques.

Typical technique	Laser pulse	Temporal resolution	Frame number	Image acquisition	Applications
M-FTOP [62]	65 fs, 800 nm	0.96 ps	4	Direct	Laser pulse characterization
STAMP [72]	70 fs, 810 nm	229 fs	6	Direct	Laser plasma; phonon dynamics
SF-STAMP [74]	70 fs, 810 nm	133 fs	25	Direct	Laser induced phase transition
CUST [80]	50 fs, 800 nm	260 fs	60	Reconstruction	Laser propagation
ADMC [81]	30 fs, 800 nm	250 fs	4	Direct	Laser plasma
OCFI [82]	10 ps, 527 nm	34 ps	4	Reconstruction	Laser plasma and electron density
SS-FDT [83]	30 fs, 800 nm	2.5 ps	5	Reconstruction	High nonlinear optical physics
THPM [90]	30 ps, 1064 nm	1.6 ns	2	Reconstruction	Laser-induced damage
FRAME [95]	125 fs, 800 nm	200 fs	4	Reconstruction	Laser pulse characterization

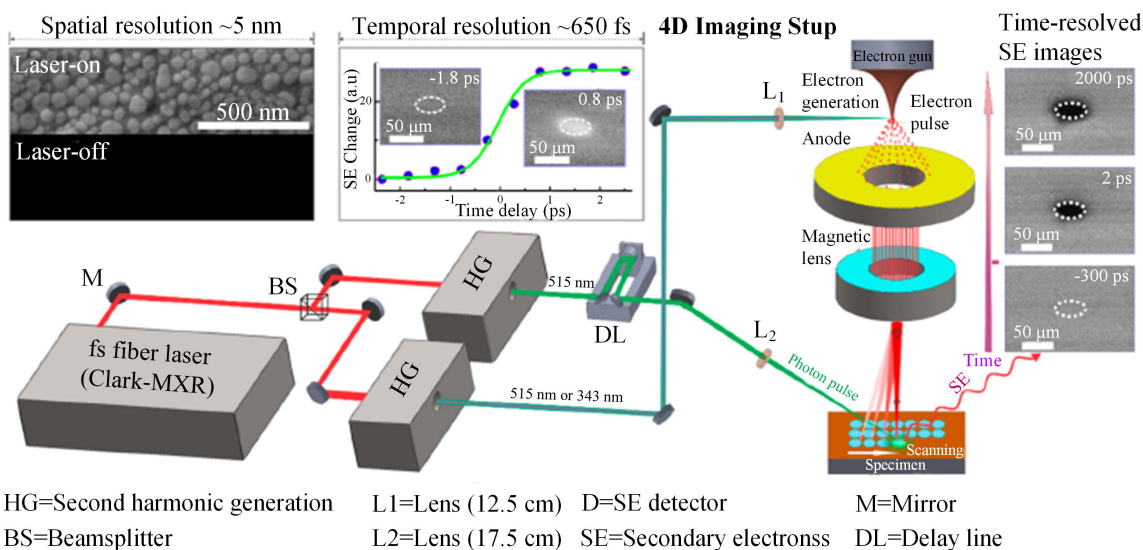


**Figure 23.** Schematic of the S-UEM experimental setup. Reprinted with permission from [96]. Copyright (2016) American Chemical Society.

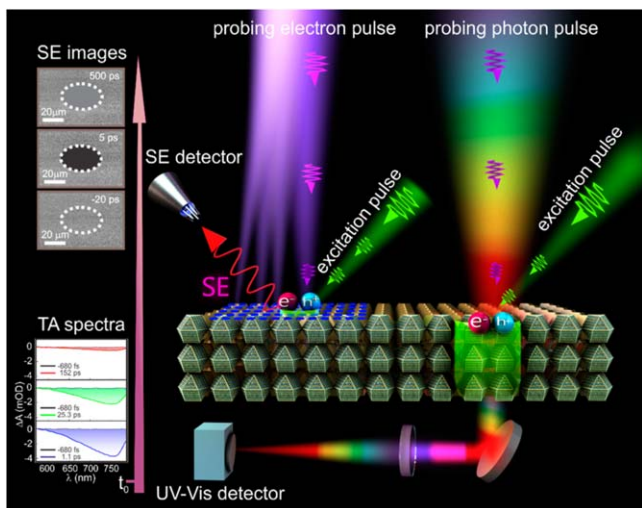


**Figure 24.** Mechanisms of the dynamics observed with the S-UEM, where the valence band electrons are promoted to the conduction band upon optical excitation. The dashed ellipse indicates the location of the laser on the specimen. Several time-resolved images at selected times are displayed to indicate contrast development. High contrast is recorded because of the energy gain, and dark contrast is recorded because of the energy loss at the center of the excited region. Reprinted with permission from [97]. Copyright (2017) American Chemical Society.

line. A positively biased Everhart-Thornley detector is used to collect the secondary electrons (SEs) emitted from the specimen. Through the imaging of gold nanoparticles using pulsed-generated photoelectrons, the spatial resolution of the S-UEM was determined to be approximately 5 nm. The temporal resolution of  $650 \pm 100$  fs was obtained by the kinetics plotted for the intensity change of the SEs from a cadmium selenide (CdSe) single crystal.

**4.2. Mechanisms of the dynamics observed with the 4D S-UEM**

One can determine the regime of dynamic probing depending on the time delay between the clocking photon pulse initiating the sample dynamics and the photoelectron probing pulse generated through photoexcitation by using a field emission gun [97]. Experimentally, a computer-controlled delay line covering the time range from  $-0.6$  to  $6.0$  ns is used to define the time axis of the acquired SE images. The differences of the SE images can be extracted by subtracting the referenced image at negative timeframe. Contrast-enhanced images can be obtained from the pump pulse irradiated and nonirradiated regions. Either ‘bright’ or ‘dark’ contrast can be observed, depending on the collected number of SEs with respect to the reference image

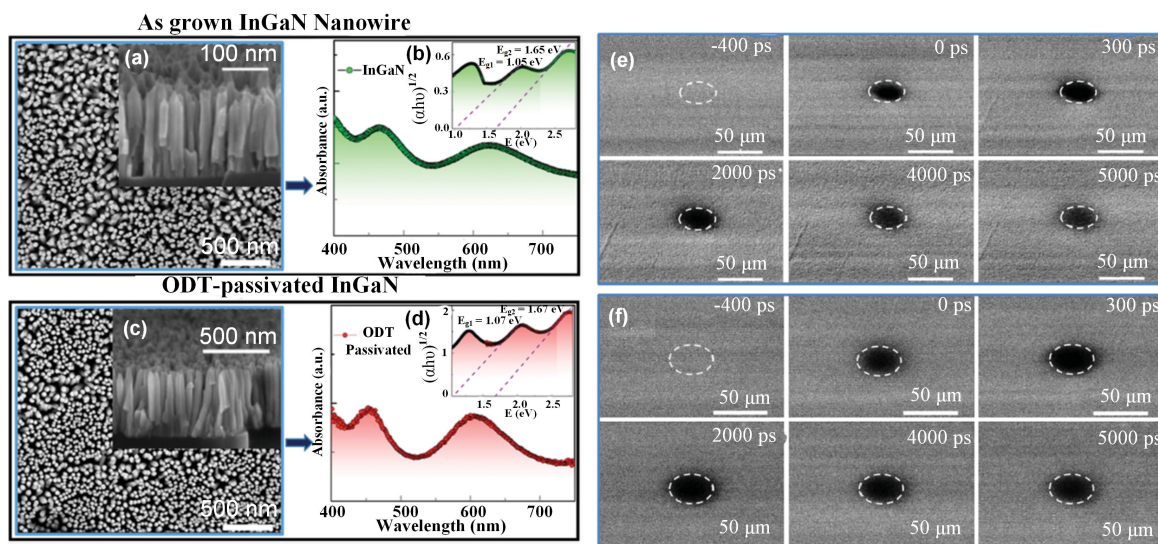


**Figure 25.** SEM images and steady-state measurements of the two samples. (a) SEM image of the surface of the as-grown NW films (cross-sectional image in the inset). (b) Absorption spectrum with the inset showing the Tauc plot. (c) SEM images of the ODT-passivated NWs (cross-sectional image in the inset). (d) Absorption spectrum with the Tauc plot in the inset. Time-resolved SE images of an InGaN NW array (e) before and (f) after surface passivation with ODT at the indicated time delays. [98] John Wiley & Sons. © 2016 WILEY-VCH Verlag GmbH & Co. KGaA, Weinheim.

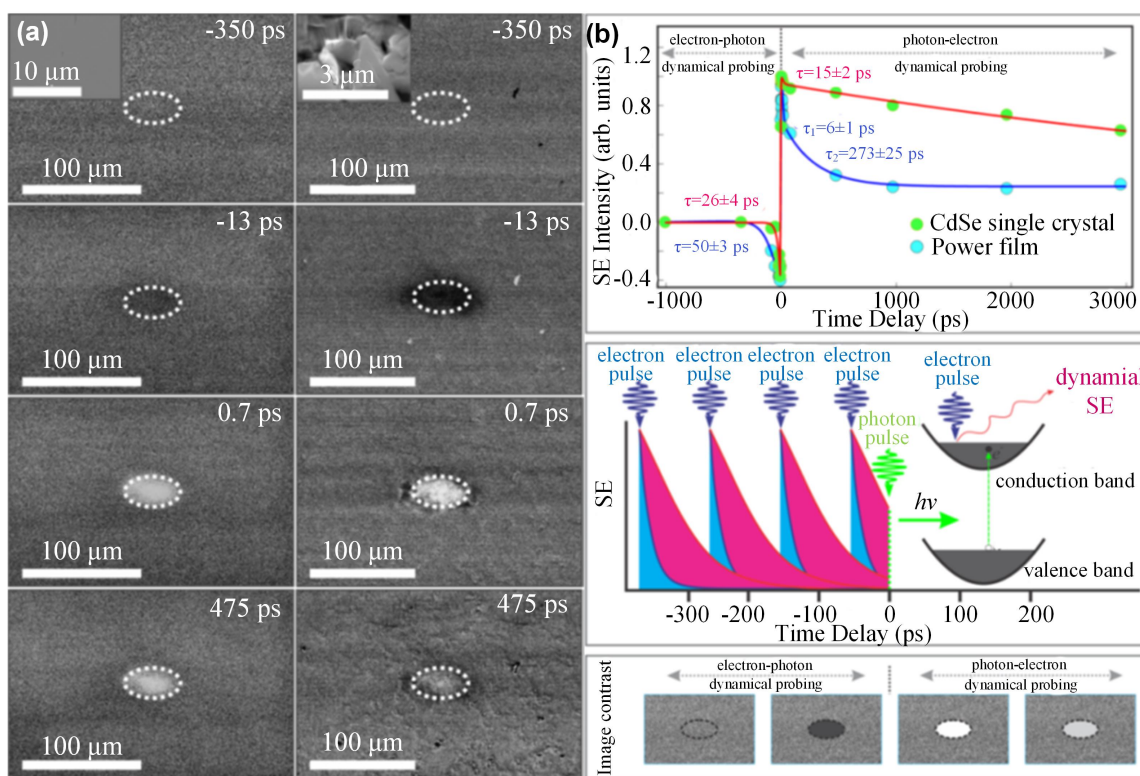


**Figure 26.** (a) Time-resolved SE images of a single crystal (left) and powder film (right) of CdSe at the indicated time delays. The SEM images, which exhibit the distinguishable morphologies of the crystal and the film, are displayed in the insets of the two topmost images. (b) Dynamics of the temporal evolution of the SE intensity for both samples. Reprinted with permission from [99]. Copyright (2015) American Chemical Society.

(figure 24). There are two probing regimes. A commonly used probing regime is called photon-electron dynamical probing, in which a clocking optical pulse arrives before the probing electron pulse. Another probing regime is called electron-

photon dynamical probing, which means that the electron pulse arrives before the clocking pulse. The two probing regimes considerably influence the nature of the image contrast that can be obtained through such time-resolved measurements.



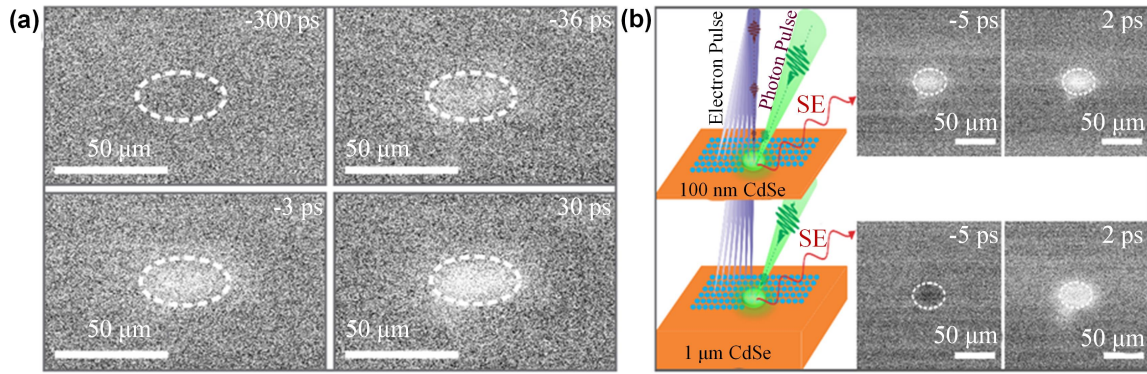


**Figure 27.** CdSe dynamics under different experimental conditions. (a) Time-resolved difference images of a CdSe (0001) single crystal in selected timeframes obtained with keV pulsed primary electrons. (b) Time-resolved difference images of 100 nm and 1 μm thick CdSe films obtained with 30 keV pulsed primary electrons. Reprinted with permission from [100]. Copyright (2017) American Chemical Society.

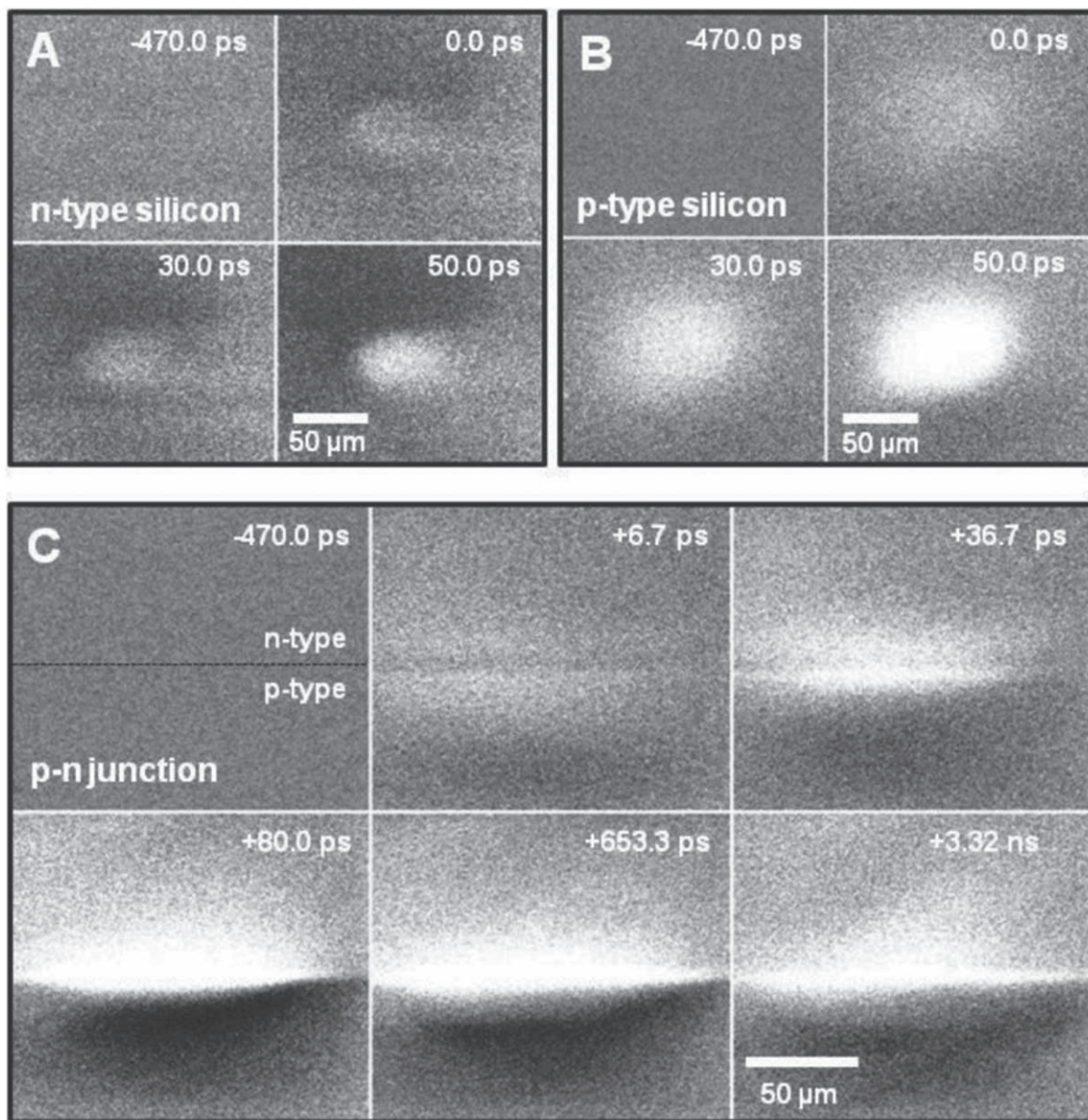


**Figure 28.** SE difference images at the indicated time delays for (a) n-type Si and (b) p-type Si. (c) SE difference images at the indicated time delays for a Si p–n junction. Reproduced with permission from [101].

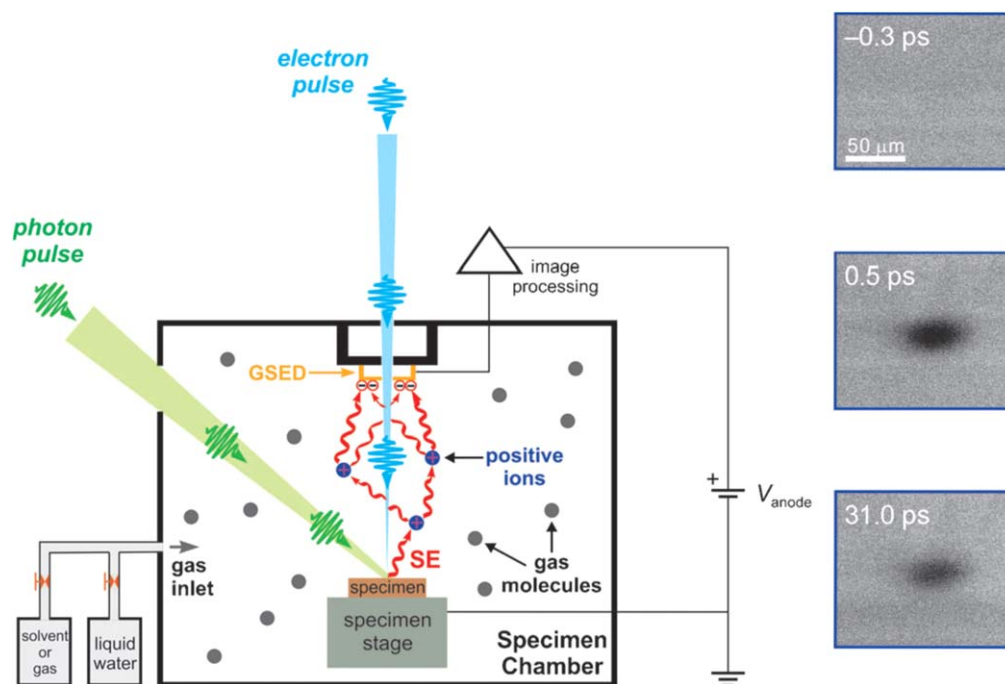


**Figure 29.** Environmental S-UEM (schematic) and three experimental frames at  $-0.3$ ,  $5.0$ , and  $31.0$  ps. The figure displays the two pulses involved, primary electron probe, and clocking optical pulse that initiates the change. [102] John Wiley & Sons. Copyright © 2013 WILEY-VCH Verlag GmbH & Co. KGaA, Weinheim.

#### 4.3. Illustrative examples

**4.3.1. Charge carrier dynamics on the surface of indium gallium nitride nanowires (NWs).** An S-UEM was employed to image the charge carrier dynamics and carrier diffusion on the surface of indium gallium nitride (InGaN) NWs [98]. The kinetics of the SE intensity evolution and time-resolved SE images indicated that carrier recombination decreased considerably from 40% to 15% on octadecylthiol (ODT) treatment within the observed time window (figure 25), which provided direct evidence of the removal of surface states and hence nonradiative carrier recombination pathways in real space and time.

**4.3.2. Effect of the morphology on the surface charge carrier dynamics.** An S-UEM was used to determine the effect of surface morphology on surface charge carrier dynamics [99]. In contrast to a single crystal of CdSe, rapid recovery of the SE signal was observed in a CdSe powder film (figure 26). This difference can be ascribed to the fact that the surface defects in the powder film can serve as fast carrier-quenching centers that considerably reduce the number of excited carriers, which results in bright contrast. This proves that surface morphology is crucial for determining the charge carrier dynamics of photoactive materials.

Furthermore, the fundamental effect of the absorber layer thickness on the charge carrier dynamics was studied [100]. Time-resolved images indicate that the dynamics of charge carriers were highly sensitive to the thickness of absorber layer, as demonstrated using CdSe films of different thicknesses as a model system (figure 27). This finding

provided the foundation for the application of an S-UEM to a wide range of devices used in materials research, and affected the optimization of photoactive materials in these devices.

**4.3.3. Charge carrier transport at the p–n junction.** An S-UEM was used to study charge carrier generation, transport, and recombination at a silicon p–n junction with a well-defined nanoscale interface [101]. Contrary to the expected range of the trusted drift-diffusion model, the separation of carriers in the p–n junction extended considerably beyond the depletion layer. Moreover, the carrier density localized across the junction over a time range of up to tens of nanoseconds depending on the laser fluence (figure 28). The observations revealed a ballistic-type motion and formed the basis of a model that accounts for the spatiotemporal density localization across the junction.

**4.3.4. Mapping surface solvation in space and time.** The ultrafast observation of solvation dynamics was realized by an S-UEM in the environmental mode at ‘wet’ material surfaces beyond the diffraction limit of visible light [102]. As prototypes for mapping surface solvation in space and time, CdSe surfaces with atomically distinct surface structures and coated with polar and nonpolar molecules were studied (figure 29). The distinct dynamic behaviors originated from the differences in interactions and structures between ambient adsorbate molecules and the surfaces involved. An S-UEM in the environmental mode can potentially be used to explore



reactivity and interfacial phenomena with the temporal and spatial scales of structural dynamics.

## 5. Summary and outlook

In summary, the developments in ultrafast chemistry and ultrafast physics have made it possible to observe and control electron dynamics in manufacturing, which is expected to considerably promote the development of basic manufacturing research. In the observation of the local instantaneous electron dynamic spatiotemporal evolution process in ultrafast laser manufacturing, the consideration of temporal and spatial resolutions and panoramic measurement at different scales are two major challenges. To address the challenges, we have reviewed the principles and applications of major ultrafast optical imaging methods, such as the pump-probe method, STAMP, CUST, THPM, FRAME, and 4D S-UEM. We have analyzed how these methods circumvent the limitations of traditional image sensors to achieve increased frame rates and shutter speeds. Although the methods trade off one or more parameters of specificity for an increased image-acquisition speed, they are complementary to each other. In the near future, a multiscale observation system with high spatial-temporal resolution and dynamic continuous observation capability could be established by combining pump detection, new ultrafast continuous imaging technology, and improved 4D S-UEM technology. Such a system could be used to determine the evolution of the structure and properties from electron ionization (femtosecond-picosecond scale) and material phase transition (picosecond-nanosecond scale) in a manufacturing activity in which the observations of multiscale processes have high spatial-temporal resolution, which would bring about a paradigm shift in femtosecond laser manufacturing.

## Acknowledgments

This study was supported by the National Natural Science Foundation of China under Grant Nos. 51975054, 61605140 and 11704028, the National Key R&D Program of China (2017YFB1104300), and Beijing Institute of Technology Research Fund Program for Young Scholars. The authors gratefully acknowledge the discussion with professor Costas Grigoropoulos from the University of California at Berkeley.

## ORCID iDs

Baoshan Guo  <https://orcid.org/0000-0002-9640-1532>

## References

- [1] Gattass R and Mazur E 2008 Femtosecond laser micromachining in transparent materials *Nat. Photon.* **2** 219
- [2] Sugioka K and Cheng Y 2014 UltraCast lasers—reliable tools for advanced materials processing *Light: Sci. Appl.* **3** 149

- [3] Kerse C, Kalaycıoğlu H, Elahi P, Çetin B, Kesim D K, Akçaalan Ö and Holzwarth R 2016 Ablation-cooled material removal with ultrafast bursts of pulses *Nature* **537** 84
- [4] Jiang L and Tsai H L 2005 Repeatable nanostructures in dielectrics by femtosecond laser pulse trains *Appl. Phys. Lett.* **87** 151104
- [5] Zhao Y, Han Q, Cheng Z, Jiang L and Qu L 2017 Integrated graphene systems by laser irradiation for advanced devices *Nano Today* **12** 14–30
- [6] Tan D, Sharafudeen K N, Yue Y and Qiu J 2016 Femtosecond laser induced phenomena in transparent solid materials: fundamentals and applications *Prog. Mater. Sci.* **76** 154–228
- [7] Yin K, Duan J A, Sun X, Wang C and Luo Z 2015 Formation of superwetting surface with line-patterned nanostructure on sapphire induced by femtosecond laser *Appl. Phys. A* **119** 69–74
- [8] Wang C, Luo Z, Duan J A, Jiang L, Sun X, Hu Y and Lu Y 2015 Adjustable annular rings of periodic surface structures induced by spatially shaped femtosecond laser *Laser Phys. Lett.* **12** 056001
- [9] Wang A, Jiang L, Li X, Liu Y, Dong X, Qu L and Lu Y 2015 Mask-free patterning of high-conductivity metal nanowires in open air by spatially modulated femtosecond laser pulses *Adv. Mater.* **27** 6238–43
- [10] Fan P, Bai B, Long J, Jiang D, Jin G, Zhang H and Zhong M 2015 Broadband high-performance infrared antireflection nanowires facily grown on ultrafast laser structured Cu surface *Nano Lett.* **15** 5988–94
- [11] Cao Y Y, Takeyasu N, Tanaka T, Duan X M and Kawata S 2009 3D metallic nanostructure fabrication by surfactant-assisted multiphoton-induced reduction *Small* **5** 1144–8
- [12] Jiang L, Wang A D, Li B, Cui T H and Lu Y F 2018 Electrons dynamics control by shaping femtosecond laser pulses in micro/nanofabrication: modeling, method, measurement and application *Light: Sci. Appl.* **7** 17134
- [13] Liang J and Wang L V 2018 Single-shot ultrafast optical imaging *Optica* **5** 1113
- [14] Hebeisen C T, Sciaini G, Harb M, Ernstorfer R, Kruglik S G and Miller R J D 2008 Direct visualization of charge distributions during femtosecond laser ablation of a Si(100) surface *Phys. Rev. B* **78** 081403(R)
- [15] Hu H, Liu T and Zhai H 2015 Comparison of femtosecond laser ablation of aluminum in water and in air by time-resolved optical diagnosis *Opt. Express* **23** 628–35
- [16] Harilal S S, Diwakar P K, Polek M P and Phillips M C 2015 Morphological changes in ultrafast laser ablation plumes with varying spot size *Opt. Express* **23** 15608–15
- [17] Anoop K K, Harilal S S, Philip R, Bruzzese R and Amoroso S 2016 Laser fluence dependence on emission dynamics of ultrafast laser induced copper plasma *J. Appl. Phys.* **120** 185901
- [18] Zhang N, Zhu X, Yang J, Wang X and Wang M 2007 Time-resolved shadowgraphs of material ejection in intense femtosecond laser ablation of aluminum *Phys. Rev. Lett.* **99** 167602
- [19] Hu H, Wang X, Zhai H, Zhang N and Wang P 2010 Generation of multiple stress waves in silica glass in high fluence femtosecond laser ablation *Appl. Phys. Lett.* **97** 061117
- [20] Zhao X and Shin Y C 2013 Coulomb explosion and early plasma generation during femtosecond laser ablation of silicon at high laser fluence *J. Phys. D: Appl. Phys.* **46** 335501
- [21] Kalupka C, Finger J and Reininghaus M 2016 Time-resolved investigations of the non-thermal ablation process of graphite induced by femtosecond laser pulses *J. Appl. Phys.* **119** 153105
- [22] Wang G, Yu Y, Jiang L, Li X, Xie Q and Lu Y 2017 Cylindrical Shockwave-induced compression mechanism in femtosecond laser pulse micro-drilling of PMMA *Appl. Phys. Lett.* **110** 161907

- [23] Sedov L I, Friedman M and Street R E 1960 Similarity and dimensional methods in mechanics *Physics Today* **13** 50
- [24] Choi T Y and Grigoropoulos C P 2002 Plasma and ablation dynamics in ultrafast laser processing of crystalline silicon *J. Appl. Phys.* **92** 4918
- [25] Zeng X, Mao X, Mao S S, Wen S B, Greif R and Russo R E 2006 Laser-induced shockwave propagation from ablation in a cavity *Appl. Phys. Lett.* **88** 061502
- [26] Jiao L S, Ng E Y K, Zheng H Y and Zhang Y L 2015 Theoretical study of pre-formed hole geometries on femtosecond pulse energy distribution in laser drilling *Opt. Express* **23** 4927–34
- [27] Zhang J, Drevinskas R, Beresna M and Kazansky P G 2015 Polarization sensitive anisotropic structuring of silicon by ultrashort light pulses *Appl. Phys. Lett.* **107** 041114
- [28] Zhang H, Colombier J P, Li C, Faure N, Cheng G and Stoian R 2015 Coherence in ultrafast laser-induced periodic surface structures *Phys. Rev. B* **92** 174109
- [29] Wang Q, Jiang L, Sun J, Pan C, Han W, Wang G, Zhang H, Grigoropoulos C P and Lu Y 2017 Enhancing the expansion of a plasma shockwave by crater-induced laser refocusing in femtosecond laser ablation of fused silica *Photonics Res.* **5** 488
- [30] Wang Q, Jiang L, Sun J, Pan C, Han W, Wang G, Wang F, Zhang K, Li M and Lu Y 2018 Structure-mediated excitation of air plasma and silicon plasma expansion in femtosecond laser pulses ablation *Research* **2018** 5709748
- [31] Lange H R, Chiron A, Ripoche J F, Mysyrowicz A, Breger P and Agostini P 1998 High-order harmonic generation and quasiphase matching in xenon using self-guided femtosecond pulses *Phys. Rev. Lett.* **81** 1611–3
- [32] Luc B 2004 Boosted propagation of femtosecond filaments in air by double-pulse combination *Phys. Rev. E* **69** 065601
- [33] Skrodzki P J, Burger M and Jovanovic I 2017 Transition of femtosecond-filament-solid interactions from single to multiple filament regime *Sci. Rep.* **7** 12740
- [34] Scheller M, Matthew S M, Mohammad A M, Cheng W, Jerome V M, Kolesik M, Polynkin P and Christodoulides D N 2014 Externally refuelled optical filaments *Nat. Photon.* **8** 297–301
- [35] Schwarz J and Diels J C 2002 Analytical solution for UV filaments *Phys. Rev. A* **65** 013806
- [36] Kosareva O G, Panov N A, Akozbek N, Kandidov V P, Luo Q, Hosseini S A, Liu W, Gravel J F, Roy G and Chin S L 2006 Controlling a bunch of multiple filaments by means of a beam diameter *Appl. Phys. B* **82** 111–22
- [37] Papeer J, Botton M, Gordon D, Sprangle P, Zigler A and Henis Z 2014 Extended lifetime of high density plasma filament generated by a dual femtosecond–nanosecond laser pulse in air *New J. Phys.* **16** 123046
- [38] Pan C, Jiang L, Sun J, Wang Q, Wang F and Lu Y 2019 The temporal-spatial evolution of electron dynamics induced by femtosecond double pulses *Japan. J. Appl. Phys.* **58** 030901
- [39] Wang F, Pan C, Sun J, Wang Q, Lu Y and Jiang L 2019 Direct observation of structure-assisted filament splitting during ultrafast multiple-pulse laser ablation *Opt. Express* **27** 100050
- [40] Jiang L and Tsai H L 2007 Modeling of ultrashort laser pulse-train processing of metal thin films *Int. J. Heat Mass Transfer* **50** 3461–70
- [41] Christensen B H and Balling P 2009 Modeling ultrashort-pulse laser ablation of dielectric materials *Phys. Rev. B* **79** 155424
- [42] Lee Y T and More R M 1984 An electron conductivity model for dense plasmas *Phys. Fluids* **27** 1273
- [43] Sun Q, Jiang H, Liu Y, Wu Z, Yang H and Gong Q 2005 Measurement of the collision time of dense electronic plasma induced by a femtosecond laser in fused silica *Opt. Lett.* **30** 320–2
- [44] Papazoglou D G, Abdollahpour D and Tzortzakis S 2014 Ultrafast electron and material dynamics following femtosecond filamentation induced excitation of transparent solids *Appl. Phys. A* **114** 161
- [45] Pan C, Jiang L, Wang Q, Sun J, Wang G and Lu Y 2018 Temporal-spatial measurement of electron relaxation time in femtosecond laser induced plasma using two-color pump-probe imaging technique *Appl. Phys. Lett.* **112** 191101
- [46] Zhang N, Zhu X, Yang J, Wang X and Wang M 2007 Time-resolved shadowgraphs of material ejection in intense femtosecond laser ablation of aluminium *Phys. Rev. Lett.* **99** 167602
- [47] Bonse J and Kruger J 2010 Pulse number dependence of laser induced periodic surface structures for femtosecond laser irradiation of silicon *J. Appl. Phys.* **108** 3
- [48] Liang F, Vallee R and Chin S L 2012 Physical evolution of nanograting inscription on the surface of fused silica *Opt. Mater. Express* **2** 900–6
- [49] Liu Y, Brelet Y, He Z, Yu L, Forestier B, Deng Y, Jiang H and Houard A 2013 Laser-induced periodic annular surface structures on fused silica surface *Appl. Phys. Lett.* **102** 251103
- [50] He S, Nivas J J J, Vecchione A, Hu M and Amoroso S 2016 On the generation of grooves on crystalline silicon irradiated by femtosecond laser pulses *Opt. Express* **24** 3238–47
- [51] Sciamanna M and Shore K A 2015 Physics and applications of laser diode chaos *Nat. Photon.* **9** 151–62
- [52] Solli D R, Ropers C, Koonath P and Jalali B 2007 Optical rogue waves *Nature* **450** 1054–7
- [53] Jalali B, Solli D R, Goda K, Tsia K and Ropers C 2010 Real-time measurements, rare events and photon economics *Eur. Phys. J. Spec. Top.* **185** 145–57
- [54] Tuchin V V 2007 Methods and algorithms for the measurement of the optical parameters of tissues *Tissue Optics: Light Scattering Methods and Instruments for Medical Diagnosis* (SPIE) pp 303–4
- [55] Poulin P R and Nelson K A 2006 Irreversible organic crystalline chemistry monitored in real time *Science* **313** 1756–60
- [56] Kodama R I, Norreys P, Mima K, Dangor A, Evans R, Fujita H, Kitagawa Y, Krushelnick K, Miyakoshi T and Miyanaga N 2001 Fast heating of ultrahigh-density plasma as a step towards laser fusion ignition *Nature* **412** 798–802
- [57] Li Z, Tsai H E, Zhang X, Pai C H, Chang Y Y, Zgadzaj R, Wang X, Khudik V, Shvets G and Downer M C 2016 Single-shot visualization of evolving plasma wake fields *AIP Conf. Proc.* **1777** 040010
- [58] Bradley D, Bell P, Kilkenny J, Hanks R, Landen O, Jaanimagi P, McKenty P and Verdon C 1992 High-speed gated x-ray imaging for ICF target experiments *Rev. Sci. Instrum.* **63** 4813–7
- [59] Muybridge J 1882 The horse in motion *Nature* **25** 605
- [60] Couairon A 2003 Light bullets from femtosecond filamentation *Eur. Phys. J. D* **27** 159–67
- [61] Couairon A and Mysyrowicz A 2007 Femtosecond filamentation in transparent media *Phys. Rep.* **441** 47–189
- [62] Wang X, Yan L, Si J, Matsuo S, Xu H and Hou X 2014 High-frame-rate observation of single femtosecond laser pulse propagation in fused silica using an echelon and optical polarigraphy technique *Appl. Opt.* **53** 8395–9
- [63] Shin T, Wolfson J W, Teitelbaum S W, Kandyla M and Nelson K A 2014 Dual echelon femtosecond single-shot spectroscopy *Rev. Sci. Instrum.* **85** 083115
- [64] Fujimoto M, Aoshima S, Hosoda M and Tsuchiya Y 1999 Femtosecond time-resolved optical polarigraphy: imaging of the propagation dynamics of intense light in a medium *Opt. Lett.* **24** 850–2
- [65] Couairon A, Sudrie L, Franco M, Prade B and Mysyrowicz A 2005 Filamentation and damage in fused silica induced by tightly focused femtosecond laser pulses *Phys. Rev. B* **71** 125435

- [66] Corkum P B and Krausz F 2013 Attosecond science *Nat. Phys.* **3** 381–7
- [67] Hassan M T, Luu T T, Moulet A, Raskazovskaya O, Zhokhov P, Garg M, Karpowicz N, Zheltikov A, Pervak V and Krausz F 2016 Optical attosecond pulses and tracking the nonlinear response of bound electrons *Nature* **530** 66–70
- [68] Jiang L, Wang A, Cao Q, Li X, Yu Y and Tan X 2014 Ultrafast laser continuous imaging device and method based on spatial time transform in frequency domain *China Patent Specification* 201410683514.1
- [69] Goda K, Tsia K and Jalali B 2009 Serial time-encoded amplified imaging for real-time observation of fast dynamic phenomena *Nature* **458** 1145–9
- [70] Lei C, Guo B, Cheng Z and Goda K 2016 Optical time-stretch imaging: principles and applications *Appl. Phys. Rev.* **3** 011102
- [71] Wu J L *et al* 2017 Ultrafast laser-scanning time-stretch imaging at visible wavelengths *Light Sci. Appl.* **6** e16196
- [72] Nakagawa K *et al* 2014 Sequentially timed all-optical mapping photography (STAMP) *Nat. Photon.* **8** 695–700
- [73] Gao G *et al* 2017 Ultrafast all-optical solid-state framing camera with picosecond temporal resolution *Opt. Express* **25** 8721–9
- [74] Suzuki T, Hida R, Yamaguchi Y, Nakagawa K, Saiki T and Kannari F 2017 Single-shot 25-frame burst imaging of ultrafast phase transition of  $\text{Ge}_2\text{Sb}_2\text{Te}_5$  with a sub-picosecond resolution *Appl. Phys. Express* **10** 092502
- [75] Suzuki T, Isa F, Fujii L, Hirokawa K, Nakagawa K, Goda K, Sakuma I and Kannari F 2015 Sequentially timed all-optical mapping photography (STAMP) utilizing spectral filtering *Opt. Express* **23** 30512–22
- [76] Gao G *et al* 2017 Ultrafast all-optical imaging technique using low-temperature grown GaAs/AlxGa1-xAs multiple-quantum-well semiconductor *Phys. Lett.* **381** 3594–8
- [77] Gabolde P and Trebino R 2008 Single-frame measurement of the complete spatiotemporal intensity and phase of ultrashort laser pulses using wavelength-multiplexed digital holography *J. Opt. Soc. Am. B* **25** A25–33
- [78] Gabolde P and Trebino R 2006 Single-shot measurement of the full spatiotemporal field of ultrashort pulses with multi-spectral digital holography *Opt. Express* **14** 11460–7
- [79] Takeda J, Oba W, Minami Y, Saiki T and Katayama I 2014 Ultrafast crystalline-to-amorphous phase transition in  $\text{Ge}_2\text{Sb}_2\text{Te}_5$  chalcogenide alloy thin film using single-shot imaging spectroscopy *Appl. Phys. Lett.* **104** 261903
- [80] Lu Y, Wong T T W, Chen F and Wang L 2019 Compressed ultrafast spectral-temporal photography *Phys. Rev. Lett.* **122** 193904
- [81] Yeola S, Kuk D and Kim K Y 2018 Single-shot ultrafast imaging via spatiotemporal division of femtosecond laser pulses *J. Opt. Soc. Am. B* **35** 2822–7
- [82] Chen G, Li J, Peng Q, Liu S and Liu J 2017 All-optical coaxial framing photography using parallel coherence shutters *Opt. Lett.* **42** 415–8
- [83] Li Z, Zgadzaj R, Wang X, Chang Y Y and Downer M C 2014 Single-shot tomographic movies of evolving light-velocity objects *Nat. Commun.* **5** 3085
- [84] Li Z, Zgadzaj R, Wang X, Reed S, Dong P and Downer M C 2010 Frequency-domain streak camera for ultrafast imaging of evolving light-velocity objects *Opt. Lett.* **35** 4087–9
- [85] Matlis N H, Reed S, Bulanov S S, Chvykov V, Kalintchenko G, Matsuoka T, Rousseau P, Yanovsky V, Maksimchuk A and Kalmykov S 2006 Snapshots of laser wakefields *Nat. Phys.* **2** 749–53
- [86] Le Blanc S, Gaul E, Matlis N, Rundquist A and Downer M 2000 Single shot measurement of temporal phase shifts by frequency-domain holography *Opt. Lett.* **25** 764–6
- [87] Nuss M C, Li M, Chiu T H, Weiner A M and Partovi A 1994 Time to-space mapping of femtosecond pulses *Opt. Lett.* **19** 664–6
- [88] Gordon R, Bender R and Herman G T 1970 Algebraic reconstruction techniques (ART) for three-dimensional electron microscopy and x-ray photography *J. Theoret. Biol.* **29** 471–6
- [89] Kak A C and Slaney M 1988 *Principles of Computerized Tomographic Imaging* (Piscataway, NJ: IEEE) (<https://doi.org/10.1118/1.1455742>)
- [90] Yue Q, Cheng Z, Han L, Yang Y and Guo C 2017 One-shot time-resolved holographic polarization microscopy for imaging laser induced ultrafast phenomena *Opt. Express* **25** 14182–91
- [91] Colomb T, Dürr F, Cuche E, Marquet P, Limberger H G, Salathé R P and Depeursinge C 2005 Polarization microscopy by use of digital holography: application to optical-fiber birefringence measurements *Appl. Opt.* **44** 4461–9
- [92] Mishchik K *et al* 2010 Nanosize structural modifications with polarization functions in ultrafast laser irradiated bulk fused silica *Opt. Express* **18** 24809–24
- [93] Sudrie L, Franco M, Prade B and Mysyrowicz A 2001 Study of damage in fused silica induced by ultra-short IR laser pulses *Opt. Commun.* **191** 333–9
- [94] Šiaulys N, Gallais L and Melninkaitis A 2014 Direct holographic imaging of ultrafast laser damage process in thin films *Opt. Lett.* **39** 2164–7
- [95] Ehn A, Bood J, Li Z, Berrocal E, Alden M and Kristensson E 2017 FRAME: femtosecond videography for atomic and molecular dynamics *Light Sci. Appl.* **6** e17045
- [96] Sun J, Adhikari A, Shaheen B S, Yang H and Mohammed O F 2016 Mapping carrier dynamics on material surfaces in space and time using scanning ultrafast electron microscopy *J. Phys. Chem. Lett.* **7** 985–94
- [97] Adhikari A, Eliason J K, Sun J, Bose R, Flannigan D J and Mohammed O F 2017 Four-dimensional ultrafast electron microscopy: insights into an emerging technique *ACS Appl. Mater. Interfaces* **9** 3–16
- [98] Khan J I, Adhikari A, Sun J, Bose R, Priante D, Shaheen B S, Ng T K, Ooi B S, Bakr O M and Mohammed O F 2016 Enhanced optoelectronic performance of a passivated nanowire-based device: key information from real-space imaging using 4D electron microscopy *Small* **12** 2313–20
- [99] Sun J, Melnikov V A, Khan J I and Mohammed O F 2015 Real-space imaging of carrier dynamics of materials surfaces by second-generation four-dimensional scanning ultrafast electron microscopy *J. Phys. Chem. Lett.* **6** 3884–90
- [100] Shaheen B S, Sun J, Yang D S and Mohammed O F 2017 Spatiotemporal observation of electron-impact dynamics in photovoltaic materials using 4D electron microscopy *J. Phys. Chem. Lett.* **8** 2455–62
- [101] Najafi E, Scarborough T D, Tang J and Zewail A 2015 Four-dimensional imaging of carrier interface dynamics in p–n junctions *Science* **347** 164
- [102] Yang D, Mohammed O F and Zewail A H 2013 Environmental scanning ultrafast electron microscopy: structural dynamics of solvation at interfaces *Angew. Chem., Int. Ed.* **52** 2897–901